



Universität Hamburg

DER FORSCHUNG | DER LEHRE | DER BILDUNG

Fakultät für Mathematik, Informatik und Naturwissenschaften Fachbereich Physik
Institut für Experimentalphysik

Bachelor Thesis

Combined Analysis of the 2019 gamma-ray flare from PG 1553+113 with Fermi-LAT and H.E.S.S.

Erstgutachter: Dr. Manuel Meyer
Zweitgutachter: Dr. Martin Tluczykont

Vorgelegt von:
Till Moritz, 7299579
Schlankreye 17, 20144 Hamburg
till.moritz@studium.uni-hamburg.de
Bachelor of Science: Physik

Abgabe:
Hamburg, 18.04.2023

Abstract

In 2019, an increase in flux was observed for the blazar PG1553+113 in the region of high-energy (HE) and very high-energy (VHE) γ radiation. This so-called flare was observed by both H.E.S.S. and *Fermi*-LAT, which together cover the energy range between ~ 20 MeV to a few TeV. Thus, these two instruments capture a large part of the second peak in the leptonic-hadronic model, which results mainly from inverse Compton scattering and the decay of π^0 -hadrons. With a redshift of $z \approx 0.433$, the spectrum of the blazar is subject to absorptions by the extragalactic background light (EBL), which is particularly evident in the range of the H.E.S.S. data.

First, the *Fermi* data will be analysed using FERMIPY, producing light curves for the whole of 2019. Flux variabilities are identified using the Bayesian block algorithm. A spectral analysis of PG1553+113 follows, using the logarithmic parabola as a spectral model. In the second part, the analysis is continued in GAMMAPY, including the H.E.S.S. data. For this step, the time period is limited to the H.E.S.S. observations.

Using GAMMAPY, a joint fit of the complete data set is created, which describes the region around the second peak of the spectral energy distribution (SED). A major advantage of this analysis is that it uses all the statistical information from both data sets. It will be found that both the Smooth Broken Power Law and the Log Parabola give a very good approximation to the generated flux points of the SED.

Zusammenfassung

Im Jahr 2019 wurde für den Blazar PG1553+113 ein Anstieg des Flusses im Bereich der hoch- (HE) und sehr hochenergetischen (VHE) γ -Strahlung registriert. Dieser sogenannte Flare wurde sowohl von H.E.S.S. als auch von *Fermi*-LAT beobachtet, die zusammen den Energiebereich zwischen ~ 20 MeV bis zu einigen TeV abdecken. Damit erfassen die beiden Instrumente einen großen Teil des zweiten Peaks im leptonisch-hadronischen Modell, der hauptsächlich aus der inversen Compton-Streuung und dem Zerfall von π^0 -Hadronen resultiert. Mit einer Rotverschiebung von $z \approx 0.433$ unterliegt das Spektrum des Blazaren Absorptionen durch das extragalaktische Hintergrundlicht (EBL), was sich insbesondere im Bereich der H.E.S.S.-Daten abzeichnet.

Die *Fermi*-Daten werden zunächst mit FERMIPY analysiert, wobei Lichtkurven für das gesamte Jahr 2019 erstellt werden. Flussvariabilitäten werden mithilfe des Bayes'schen Blockalgorithmus identifiziert. Unter Verwendung der logarithmischen Parabel als Spektralmodell folgt eine Analyse des Spektrums von PG1553+113. Im zweiten Teil wird dies in GAMMAPY fortgesetzt, wobei die H.E.S.S.-Daten in die Analyse mit einbezogen werden. Für diesen Schritt wird der Zeitraum auf die H.E.S.S.-Beobachtungen begrenzt.

Mit Hilfe von GAMMAPY wird nun ein gemeinsamer Fit des vollständigen Datensatz erstellt, welcher den Bereich um den zweiten Peak der spektralen Energieverteilung (SED) beschreibt. Ein großer Vorteil dieser Analyse ist, dass dabei alle statistische Informationen beider Datensätze genutzt werden. Es wird sich herausstellen, dass sowohl das glatt gebrochene Potenzgesetz, als auch die logarithmische Parabel eine sehr gute Annäherung an die erzeugten Flusspunkte der SED liefern.

Contents

1	Introduction	1
2	Production of High Energy and Very High Energy γ-Rays	3
2.1	Leptonic Model	4
2.2	Hadronic Model	5
2.3	Sources of Astrophysical γ -rays	6
2.3.1	Active Galactic Nuclei	6
2.3.2	The Blazar PG 1553+113	9
2.4	Extragalactic Background Light (EBL)	10
3	γ-ray Instruments	11
3.1	<i>Fermi</i> Large Area Telescope	12
3.1.1	Point Spread Function and Instrument Response	13
3.2	Imaging Air Cherenkov Telescopes	14
3.2.1	High Energy Stereoscopic System (H.E.S.S.)	16
4	Analysis Methodology	17
4.1	Maximum Likelihood Analysis	17
4.2	PS Analysis Method	18
4.3	Spectral Models	19
4.4	FERMIPY and GAMMAPY Package	21
5	Analysis	23
5.1	<i>Fermi</i> Data Analysis with FERMIPY	23
5.1.1	Setup	24
5.1.2	Spectral Energy Distribution	26
5.1.3	Light Curves	27
5.2	<i>Fermi</i> and H.E.S.S. Data Analysis with GAMMAPY	30
5.2.1	<i>Fermi</i> Analysis	30
5.2.2	H.E.S.S. Analysis	31
5.2.3	Combined Analysis of <i>Fermi</i> and H.E.S.S. Data	33
6	Conclusion	37
	List of figures	39
	List of tables	40
	References	41
	Appendix	45

List of Abbreviations

AGN	–	Active Galactic Nucleus
CMB	–	Cosmic Microwave Background
CR	–	Cherenkov Radiation
CsI	–	Caesium Iodine
CTA	–	Cherenkov Telescope Array
DRM	–	Detector Response Matrix
EBL	–	Extragalactic Background Light
EC	–	External Compton
EDISP	–	Energy Dispersion
FGL	–	<i>Fermi</i> Gamma-ray LAT
HE	–	High Energy
H.E.S.S.	–	High Energy Stereoscopic System
IACT	–	Imaging Air Cherenkov Telescope
IC	–	Inverse Compton
IRF	–	Instrument Response Function
LAT	–	Large Area Telescope
Ly- α	–	Lyman-alpha
PSF	–	Point Spread Function
QSO	–	Quasi Stellar Object
SED	–	Spectral Energy Distribution
SSC	–	Synchrotron Self-Compton
TS	–	Test Statistic
UV	–	Ultraviolet
VHE	–	Very High Energy

1 Introduction

Over centuries, humankind has observed the sky and its countless luminous objects with great curiosity. For a long time, these observations were limited exclusively to light in the optical spectrum, but over time telescopes have been developed that are sensitive to a much broader range of energy. Nowadays, various Ground- and Space-based instruments can detect lower-energy radiation, such as radio waves and microwaves, but also ultraviolet light and X-rays with higher energy [Goddard Space Flight Center 2013]. The most energetic form of electromagnetic waves are γ -rays with energies > 100 keV (10^5 eV). The study of this radiation is important for various questions in science. Dark matter, for example, could be detected indirectly by so-called self-annihilation, in which the energy is emitted in the form of radiation. A candidate of dark matter could also be axions that cause distortions in the energy spectrum of distant galaxies through photon-axion oscillation in extragalactic magnetic fields. It is also hoped to find answers about the origin of cosmic rays, the highest energetic particles in the universe. Furthermore, relativistic outflows of γ -ray sources, so-called jets, are not yet fully understood. Due to the high-energetic spectrum the formation processes within these jets can be investigated further [Funk 2015].

The γ -ray background detectable on Earth consists predominantly of radiation produced in sources within our galaxy, primarily at the galactic centre. Outside the galactic plane, however, other sources were discovered in 1962. They appeared to be star-like objects but showed extreme radio emissions and could therefore not be classified as stars [Becker 2008]. It was also found that these radio sources had a large red shift, indicating a very large distance. Due to their unknown properties, the newly discovered sources were initially referred to as quasi-stellar objects (QSOs). Today it is known that QSOs are indeed distant galaxies with an Active Galactic Nucleus (AGN) consisting of a large black hole actively accreting matter from a surrounding accretion disk [Romero et al. 2018]. AGNs represent the largest number of γ -ray sources discovered so far. Since some of these objects are really distant, e.g. the blazar PKS 0537-286¹ with red shift $z > 3.1$, corresponding to a distant of more than 11.7 billion light-years, they can be used to investigate the intervening space. This is important, for example, to identify the intergalactic magnetic and photon radiation fields in the universe [Funk 2015].

A few of the AGN eject accreted matter in the form of collimated jets. When the jet is directed towards Earth, the AGN is classified as a blazar [Hinton and Hofmann

¹https://ned.ipac.caltech.edu/byname?objname=PKS+0537-286&hconst=67.8&omegam=0.308&omegav=0.692&wmap=4&corr_z=1

[2009]. In the jets, particles are accelerated highly relativistically, with suspected cosmic ray energies of up to $E_{CR} \sim 10^{21} eV$ [Becker 2008]. Through leptonic and hadronic processes, the accelerated particles generate γ -rays, producing a significant spectrum. In the high energy (HE) and very high energy range (VHE), the emission is dominated by Inverse Compton (IC) scattering of electrons on photons, as well as the decay of neutral charged pions [Funk 2015]. The blazar PG1553+113 is characterised by a particularly steep spectrum in this energy region.

Due to fluctuations in the accretion of matter, blazars show variations in the emitted photon flux. In 2019, PG1553+113 showed particularly high activity, leading the ground-based γ -ray telescope H.E.S.S. to observe the blazar [de Naurois and H. E. S. S. Collaboration 2019]. This so-called flare was also observed by the *Fermi* Space Telescope, which permanently orbits the Earth.

In this work, the γ -ray flare in 2019 will be discussed using the data from H.E.S.S. and *Fermi*. For this purpose, the theoretical basics are described in the first part, including a brief explanation of the production of γ -rays. In addition, the two telescopes and the analysis methods will be presented.

The second part of this thesis starts with the analysis of the data collected by *Fermi*-LAT for the entire year of 2019 using FERMIPY. For this purpose, the light curve for the year 2019 will be constructed to illustrate the variability of the source by summarising all detected events in weekly bins. The Bayesian block algorithm is used to identify flux variability. In the further analysis, the spectrum of PG1553+113 will be investigated by creating the spectral energy distribution (SED). The SED will be produced once for the entire year 2019, but also for the shorter period of the H.E.S.S. observations, to allow a combined analysis with the *Fermi* and H.E.S.S. data.

At this point GAMMAPY is used to continue the spectral analysis. First, the calculation of the SED for the *Fermi* data is repeated and compared with that of FERMIPY. Subsequently, the H.E.S.S. data of the γ -ray flare will be used to calculate the SED for higher energies. In this step, the Log Parabola is also used as a spectral model, taking into account absorption through the extragalactic background light (EBL). Finally, a combined fit is to be created using both data sets. In addition to the Log Parabola, the fit is also created with a Smooth Broken Power Law. The goal here is to see how GAMMAPY performs with the analysis of multiple instruments over a wide energy range.

2 Production of High Energy and Very High Energy γ -Rays

A large flux of particles generated by various astrophysical processes is constantly entering the atmosphere of the Earth. In the energy regime between 1 GeV (10^9 eV) and 10 TeV (10^{13} eV) the most frequently detected particles are protons, followed by positrons and electrons. Electron volt (eV) is a unit of energy and is defined as the kinetic energy gained by an electron, with elementary charge e , when accelerated with a voltage of 1 V [Stern 2003, chapter 13]. Figure 1 shows the energy flux of different particles over a large energy range. The data was compiled

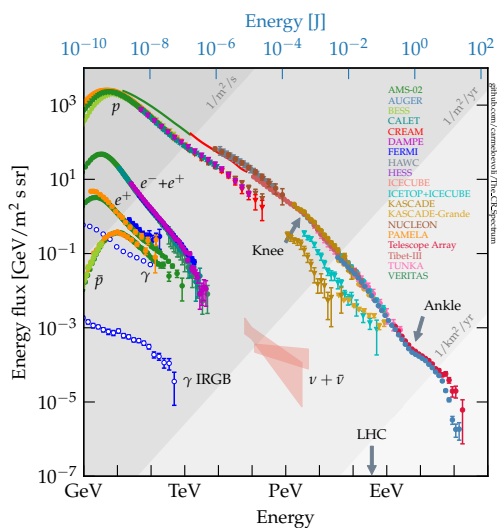


Figure 1: The cosmic ray spectrum detectable on Earth measured with various instruments [Evoli 2020]

from different experiments. As mentioned above, γ rays are the most energetic form of electromagnetic radiation. Sources of γ -ray emission occur as both galactic and extragalactic objects. Sources within our galaxy are responsible for most of the flux detectable on earth. In particular, these are pulsars, pulsar wind nebulae, supernova remnants, compact object binary systems, and the galactic center, which all lie predominantly in the galactic plane. Extragalactic objects are starburst galaxies, γ -ray bursts and active galactic nuclei (AGN) [Degrange and Fontaine 2015]. The γ -ray background can be seen in figure 4. AGNs are the most powerful steady source of γ -ray due to relativistic outflows (jets) produced by some of these active galactic nuclei. If a jet is directed towards Earth, the AGN is classified as a blazar, and since AGNs are usually very distant, blazars are the most frequently observed objects of this type. Due to the distance and the limited resolution of the γ -ray telescopes they appear point-like [Hinton and Hofmann 2009]. It is believed that through acceleration processes, charged cosmic rays up to energies of $E_{CR} \sim 10^{21}$ eV are generated within the jets. The spectrum of the cosmic rays can be described by a power law $dN/dE \sim E^{-\Gamma}$ (see section 4.3 for more detail) [Funk 2015]. Due to deflection of charged particles in intergalactic magnetic fields the exact origin of the accelerated particles cannot be determined. This counts especially for particles with energies $< 10^{17}$ eV [Becker 2008]. However the AGN not only generate high-energetic charged particles such as protons and electrons. These

particles, in turn, produces γ -rays through hadronic and leptonic emission over a broad spectrum. As they are neutrally charged electromagnetic waves, they are not influenced by magnetic fields. The mechanisms of hadronic and leptonic emission is explained in the following section.

2.1 Leptonic Model

The leptonic model describes the emission of radiation based on the acceleration of electrons or positrons. There are two leptonic processes that emit γ -rays in different energy ranges. The synchrotron radiation appears when relativistic charged particles move inside a magnetic field. The electromagnetic waves arise tangential to the direction of motion and their energy can be described by the following equation [Funk 2015],

$$E_{\text{sync}} = 0.2 \text{ eV} \frac{B}{10\mu\text{G}} \left(\frac{E_e}{1 \text{ TeV}} \right)^2 \quad (1)$$

with the magnetic field B and the energy of the electrons E_e . One other possible process is Inverse Compton scattering (IC). Here the electrons scatter off target photons from radiation fields, the so-called *seed photon fields*. In this process the energy of the electrons is transferred to the photon. One scattering field is the synchrotron photon field, which is generated by the same accelerated electrons/positrons. This process is therefore also called synchrotron self-compton (SSC) [Joshi, Marscher, and Böttcher 2014]. Electrons can also be scattered by external fields such as the Cosmic Microwave Background (CMB) and the far infrared excess. This is known as external Compton scattering (EC) [Aharonian et al. 2004]. The IC scattering produces a broad spectrum of high-energetic photons. The energy of the peak of this distribution can be determined from the energies of the photon E_{ph} and the electron E_e [Funk 2015]:

$$E_{\text{IC}} = 5 \times 10^9 \text{ eV} \frac{E_{ph}}{10^{-3}\text{eV}} \left(\frac{E_e}{1 \text{ TeV}} \right)^2 . \quad (2)$$

The left diagram in figure 2 shows the spectral energy distribution (SED) for the leptonic emission over a large energy range. The spectrum of the accelerated electrons at the injection is shown as a power law (light grey), assuming a spectral index of $\alpha_{\text{injected}} = 2$. The dashed line also shows the spectrum of electrons, with a high energy cut-off at ~ 1.2 TeV due to radiative cooling. In addition, the spectra of the synchrotron radiation and IC scattering are shown (brown). Both spectra result from the spectrum of the accelerated electrons, which makes the cooling break of the electron spectrum apparent as the peak of the synchrotron and the IC spectrum. The

break also causes a change of the spectral indices (Γ_{sync} and Γ_{IC}) in the synchrotron and in the IC scattering spectrum. Both spectra have a slope of $\Gamma = (\alpha_{\text{injected}} + 1)/2$ for small energies. After the peak, the synchrotron index changes to $\Gamma_{\text{sync}} = 2$ and then drops rapidly for higher energies due to the decreasing differential cross section (Klein-Nishina turnover).

To summarise, synchrotron radiation accounts for most of the leptonic emission produced by the electron spectrum. In the energy range of 10 - 100 MeV, there is an overlap with radiation through IC scattering, which predominates in the very high energy range.

2.2 Hadronic Model

The initial particles in the hadronic model are accelerated protons. In this so-called photoproduction, high-energy protons interact with photons produced by the accelerated electrons (synchrotron radiation and bremsstrahlung) [De Angelis and Mallamaci 2018]. In these interactions, γ -rays as well as neutrinos can be produced. Possible decays are π^0 , π^+ and π^- in approximately equal proportions, with other decay products also being produced. The pions subsequently decay further, with the π^0 turning into a photon pair [Unbehaun 2020]. The π^0 thereby produces γ -rays with a minimum energy of $E_\gamma = m_{\pi^0}c^2/2 = 67.5$ MeV:

$$\pi^0 \longrightarrow \gamma + \gamma. \quad (3)$$

The charged pions decay first into muon neutrino pairs. The muons then into further neutrinos and electrons or positrons:

$$\pi^+ \longrightarrow \mu^+ + \nu_\mu, \quad \mu^+ \longrightarrow e^+ + \nu_e + \bar{\nu}_\mu, \quad (4)$$

$$\pi^- \longrightarrow \mu^- + \bar{\nu}_\mu, \quad \mu^- \longrightarrow e^- + \bar{\nu}_e + \nu_\mu. \quad (5)$$

The resulting electrons and positrons also generate γ -rays through synchrotron radiation. The right-hand diagram in figure 2 shows the SED for the hadronic emission, including the spectrum of the accelerated protons. A spectral index of $\alpha_{\text{injected}} = 2$ is assumed here equivalent to the electron spectrum. In addition, one can see the γ -ray spectrum produced by the π^0 decay in the high energy range, with a spectral index of $\alpha = 2$ (brown) as well as for other spectral indices (thin brown). For small energies the hadronic emission is produced by synchrotron radiation of the secondary electrons (brown). Because of the leptons produced in the hadronic decay, which further produce radiation as secondary particles, this model is also called

the lepto-hadronic model [Romero et al. 2018]. Another source of radiation in this model is bremsstrahlung, which is produced by electrons.

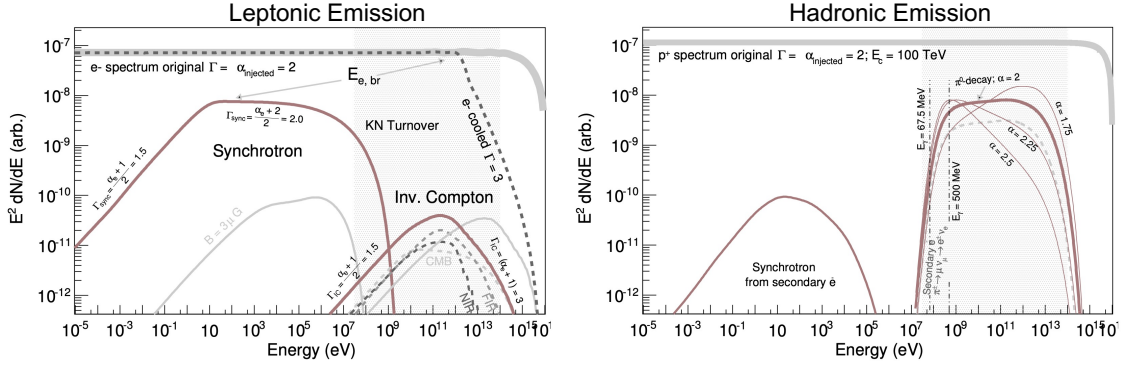


Figure 2: Left: SED of the accelerated electrons (light grey) and the resulting spectra of the synchrotron radiation and IC scattering (brown) **Right:** SED of the accelerated protons (light grey) and the spectra of the π^0 decay and synchrotron radiation of the secondary electrons (brown). Additionally the sensitive range of current γ -ray instruments (*Fermi*-LAT, IACTs) is shown (shaded grey region) [Funk 2015]

In summary, gamma rays are produced by the interaction of accelerated hadrons and leptons with interstellar magnetic (synchrotron radiation) and radiation fields (IC scattering and proton-photon interaction), as well as interstellar matter (pion decay and bremsstrahlung) [Funk 2015].

2.3 Sources of Astrophysical γ -rays

As mentioned in the introduction, several sources were discovered in 1962 that appeared as star-like objects. However, these objects showed extreme radio emission that could not be produced by any source from our Galaxy. A year later, M. R. Schmidt [1963] first suggested that the object 3C 273, with a large redshift, was a distant galaxy. Today it's known that QSOs can be classified as AGNs, which consist of a supermassive black hole that actively absorbs matter from a surrounding accretion disk [Becker 2008]. In the following section the principle of AGNs will be discussed.

2.3.1 Active Galactic Nuclei

Active galactic nuclei are located in the center of galaxies and consist of a rotating supermassive black hole ($M_{\text{BH}} \sim 10^6$ to $10^9 M_{\odot}$) and a surrounding accretion disk. The term "active" refers to the black hole's ability to accumulate matter from its surroundings and actively accelerate it, sometimes forming so-called jets. The

amount of this accretion varies, as reflected in source flux variability at all wavelengths. The variability patterns are often complex and vary for different energy ranges. The power with which the black hole accretes matter from the accretion disk is described by,

$$L_{\text{accr}} \equiv \dot{M}c^2 = q_{\text{accr}}L_{\text{Edd}} \approx 1.3 \times 10^{46} q_{\text{accr}} \left(\frac{M_{\text{BH}}}{10^8 M_{\odot}} \right) \text{erg s}^{-1} \quad (6)$$

with \dot{M} the mass accretion rate, M_{\odot} the solar mass and the dimensionless parameter q_{accr} . Furthermore, Eddington luminosity L_{Edd} describes the maximal luminosity due to the accretion of matter. As described, some AGNs form collimated jets in which the accreted matter is accelerated and thus ejected again. The jets are directed in opposite directions, so that in such a case the outflow occurs symmetrically in two directions. The power of each jet can be calculated from L_{accr} ,

$$L_{\text{jet}} = \frac{1}{2} q_{\text{jet}} L_{\text{accr}} \quad (7)$$

where $q_{\text{jet}} < 1$ [Romero et al. 2018]. The acceleration within the jets is very strong, even though the principle of operation of a jet has not yet been explained in detail. One possible explanation is that the charged particles are accelerated via shock waves. In this process, the particles pass through the collision-free shock fronts from the so-called downstream to the upstream region. However, the charged particle usually cannot overcome the magnetic potential of the shock front during the first pass. Due to this reflection at the potential, it passes the shock front again (from upstream to downstream), and the particle gains velocity. In the case of multiple reflections, the particle can be accelerated significantly. For further information see Matthews, Bell, and Blundell 2020. According to section 2.1 and 2.2, accelerated leptons and hadrons produce γ -rays over decay, bremsstrahlung, IC scattering and synchrotron radiation. Figure 3 summarizes the described processes within the AGN. In particular, the radiation processes are shown.

An important characteristic of AGN is the variability of its flux in time. The photon flux is defined as the number of photons per second per unit area. Interestingly, the fluctuations in the emitted radiation occur randomly. Although the variabilities are distributed in a certain spectrum that can be measured over a long period of time, this does not allow the prediction of the next fluctuation period. The spectral distribution follows a power law $PSD \sim \omega^{-\beta}$, where ω is the frequency of the variabilities and β is the index. The color noise of blazars for HE and VHE is

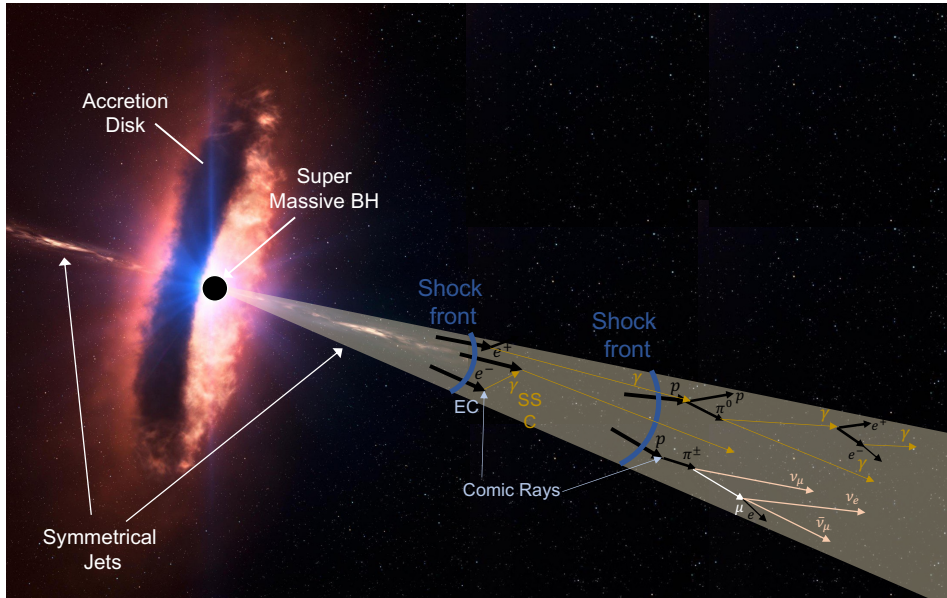


Figure 3: Schematic illustration of a blazar with a black hole and the surrounding accretion disk. In the forming jets, cosmic rays are accelerated ultrarelativistically and produce a broad band of radiation through lepto-hadronic processes.

usually between pink ($\beta = 1$) and red noise ($\beta = 2$) [H.E.S.S. Collaboration [2016](#)]. The variability of AGNs is an important indication of the size of their emission region. Due to its expansion, the light emitted by the source at any given time is measurable for at least the time it takes the light to travel the radius R of the source. On Earth, we first detect the light emitted over the shortest distance and, after a certain time, the light that has traveled the longest distance. The length of a flux variation is minimally equal to period in which all photons reach us from the time of the variation. By using this variation time the radius of emission region can be estimated approximately with $R \sim c \cdot t_{\text{var}}$ (with c as the speed of light) [The Open University [2019](#)]. This is an estimate of the observed emission region. In the co-moving reference frame, this region may be larger due to time dilation. The flux variability ranges from several months or years, but in some cases only a few minutes [Abramowski et al. [2015](#)]. These variability time spans correspond to radii of the order of magnitude of the solar system.

AGNs can be divided in two classes, the radio loud galaxies, predominantly elliptical and the radio quiet galaxies that mostly are spiral galaxies. Radio loud galaxies, which make up about 10% of AGNs, are the type where jets occur. These in turn are divided into low luminosity and high luminosity objects with $L_{\nu} = 2.5 \times 10^{26} \text{ W Hz}^{-1}$ as critical value. If the jets are directly pointed to the observer AGNs are classified

as blazars. Flat Spectrum Radio Quasars (FSRQ) represents blazars with high luminosity while BL Lacertae (BL Lac) objects describes those with low luminosity [Becker 2008]. Due to the peak in the synchrotron emission, BL Lacs are categorized as low, intermediate and high energy cutoff objects. The classification is split by the peak frequency in LBL ($\nu_{\text{peak}} < 10^{14}$ Hz), IBL (10^{14} Hz $< \nu_{\text{peak}} < 10^{15}$ Hz) and HBL ($\nu_{\text{peak}} > 10^{14}$ Hz) [Abdo et al. 2010]

2.3.2 The Blazar PG 1553+113

PG 1553+113 was discovered by Green, M. Schmidt, and Liebert 1986, who classified it as a BL Lac object with detected radio emission and rapid optical variability. The coordinates of PG 1553+113 are $\alpha_{J2000} = 15^h55^m43.04^s$, $\delta_{J2000} = 11^\circ11'24.4''$ ², which is located in the Serpens Caput constellation [Abramowski et al. 2015]. Figure 4 shows the γ -ray background in our Universe for energies above 1 GeV in the form of a sky map. The data were obtained with *Fermi*-LAT over 60 months of observations. It turns out that our galaxy is the main source of γ radiation, especially the galactic centre. Outside the galactic plane, only a few very bright sources can be seen. All known blazars are highlighted in the figure, including PG1553+113.

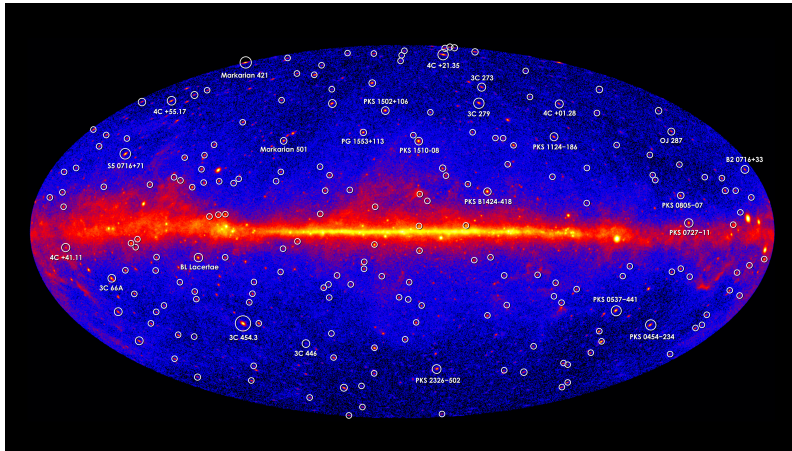


Figure 4: All sky γ -ray map of *Fermi*-LAT for 60 months containing energies $E_\gamma > 1$ GeV Source: <https://svs.gsfc.nasa.gov/11342>

Nowadays it is known that the AGN has a high frequency peak in the synchrotron radiation, which makes it a HBL. PG1553+113 was detected by H.E.S.S at very high energies (VHE, $100 \text{ GeV} < E < 30 \text{ TeV}$) and by *Fermi*-LAT at high energies (HE, $100 \text{ MeV} < E < 300 \text{ GeV}$), see section 3 for the γ -ray instruments. During the analysis of the spectrum, a peculiarity was discovered. A photon index in the VHE

²https://ned.ipac.caltech.edu/byname?objname=PG+1553%2B113&hconst=67.8&omegam=0.308&omegav=0.692&wmap=4&corr_z=1

region of $\Gamma = 4.0 \pm 0.6$ and in the HE region of $\Gamma = 1.68 \pm 0.03$ makes PG1553+113 the source with the largest ever measured spectral break between HE and VHE radiation [Abramowski et al. 2015]. The models with which the spectrum of AGN are described are explained in section 4.3.

The name PG 1553+113 is based on the catalog of quasi-stellar objects from [Hewitt and Burbidge 1987]. The Blazar can also be found under the name 4FGL J1555.7+1111 given in context of the fourth catalog of sources that was detected within the first 8 years of *Fermi*'s mission. The name is a combination of *Fermi* Gamma-ray LAT (FGL) and it's equatorial coordinates [Abdollahi et al. 2020].

2.4 Extragalactic Background Light (EBL)

The EBL is the total light emitted by all sources during the lifetime of the universe, as well as the light from the diffuse background (except the Cosmic Microwave Background (CMB)). It thus comprises the energy generated by nuclear and gravitational processes since the epoch of recombination. The emitted energy is stored in the form of an intergalactic radiation field. The spectrum of the EBL spans the wavelength region from 0.1 to 1000 μm . Due to photon-photon interactions, the EBL forms an absorption source for γ -rays. This opacity can be used to study both the intrinsic spectrum of blazars and the intensity of EBL [Dwek and Krennrich 2013].

The interaction occurs between high-energy γ -rays from a blazar, γ_{BL} , and the low-energy photons from the EBL, γ_{EBL} . In this process, the annihilation of the two photons creates an electron-positron pair that ultimately causes the absorption of the radiation [Fermi-LAT Collaboration et al. 2018]:

$$\gamma_{\text{BL}}\gamma_{\text{EBL}} \longrightarrow e^+ + e^-. \quad (8)$$

The absorption of the EBL is characterized by the optical depth $\tau_{\gamma\gamma}(E, z)$. It depends on the distance to the source (at redshift z) and the energy of the radiation, E . For further information, see Dwek and Krennrich 2013. The absorption of the EBL is described by an exponential function with $\tau_{\gamma\gamma}$ as the argument. Using this term the observed spectrum of an intergalactic source results in the following equation,

$$\left(\frac{dN}{dE}\right)_{\text{obs}} = \left(\frac{dN}{dE}\right)_{\text{int}} e^{-\tau_{\gamma\gamma}(E, z)} \quad (9)$$

with $(dN/dE)_{\text{int}}$ as the intrinsic spectrum. Due to the spectrum of the EBL, the absorption of γ rays varies with their energy E and the distance of the source (with red shift z). The cross section, $\sigma_{\gamma\gamma}(E, \epsilon, \theta, z)$ of the collision also plays an important

role, as this is an essential component in the calculation of the optical depth. It depends on the red shift, but also on the energy and angle of the two photons. Figure 5 shows the intensity of the EBL for different wavelengths, as well as the optical depth for different redshifts in the energy range between 0.1 and 100 TeV. The figure illustrates the relationship between the EBL spectrum and the energy dependence of the opacity. The increase in photon density of the EBL in the UV-optical region (0.1 to $\sim 1 \mu\text{m}$) corresponds to the increasing $\tau_{\gamma\gamma}$ between 10 and 500 GeV. After the peak, the EBL intensity decreases for $\lambda < 15 \mu\text{m}$, resulting in a less rapid rise in optical depth between 1 and ~ 10 TeV. The increase in EBL for $E_\gamma > 10$ TeV can be explained by the increase in EBL toward the peak of dust emission at $\sim 100 - 200 \mu\text{m}$ [Dwek and Krennrich 2013].

According to De Angelis and Mallamaci 2018, the EBL represents the main cause of γ -ray absorption in the energy range between $10 \text{ GeV} \leq E < 10^5 \text{ GeV}$. For higher energies, the interaction with the CMB ($10^5 \text{ GeV} \leq E < 10^{10} \text{ GeV}$) and the radio background ($E \geq 10^{10} \text{ GeV}$) are the main sources of the opacity in the Universe.

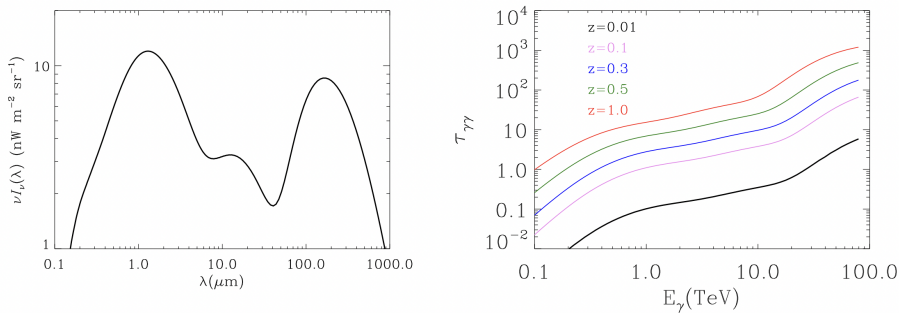


Figure 5: Left: EBL intensity versus wavelength at $z = 0$ **Right:** Optical depth for different red shifts. The figure shows the correlation between the EBL intensity and the optical depth. Source: Dwek and Krennrich 2013

3 γ -ray Instruments

The analysis in this work is based on two different γ -ray Instruments observing the sky and collecting data. The *Fermi*-LAT, which is constantly orbiting the earth as a satellite, and H.E.S.S., a ground based Cherenkov Telescope array. Both will be briefly presented in this chapter.

3.1 *Fermi* Large Area Telescope

The *Fermi* Gamma-ray Space Telescope was launched on June, 11 2008 by the NASA. The satellite constantly orbits the earth at an altitude of ~ 565 km. In about 3 hours, each source is observed by *Fermi* for approximately 30 minutes, with the satellite orbiting the Earth twice [Abramowski et al. 2015].

Figure 6 shows a visualisation of the Space Telescope in the orbit of the earth. The primary instrument of *Fermi* is the high-energy γ -ray telescope *Fermi*-LAT (Large Area Telescope). It is detecting photons in the energy range between ≈ 20 MeV to > 300 GeV. The LAT is located on top of the satellite and is turned away from Earth. The following description of the working principle of *Fermi*-LAT is based on [Atwood et al. 2009].

The telescope can reconstruct the direction and measure the energy and arrival time of the incoming γ -rays. For this purpose, the LAT consists of a 4x4 array of modules, each divided into two different detectors. The Converter-Tracker forms the upper part of the detector. Inside the tracker are 16 planes of tungsten, a high-Z material. When entering the telescope the photons may interact with the material and convert into an electron-positron pair. The planes are interleaved with silicon-strip detectors which record the path of the charged particles. The direction of the γ -ray can be reconstructed from the total momentum of the scattered e^+e^- pair. After passing the Converter-Tracker the electrons and positrons enter

the bottom part of the detector, the calorimeter. It measures the energy of the incoming γ -ray by the shower it induces. Each of the 16 modules contains 96 CsI crystals which are arranged in eight layers on top of each other, with each layer rotated by 90° with respect to its neighbors. Due to the high number of crystals, the energy of the shower is distributed over several crystals. Thus, in addition to the energy measurement, the direction of the shower can also be reconstructed. The calorimeter's ability to image showers and the depth of the detector allow measurement of a high-energy range. In addition, the background can be filtered out in this process by only considering measurements of those detector strips that lie within the showers.

Another important part of the Large Area Telescope is the Anticoincidence Detector. Its task is to filter out incoming charged particles. This detector encases the



Figure 6: Illustration of the *Fermi* Space Telescope in orbit of the earth. Source: <https://fermi.gsfc.nasa.gov>

array of Converter-Tracker and Calorimeter modules. Each time a charged particle is encountered, the coincidence detector rejects the measurement and excludes it from the data.

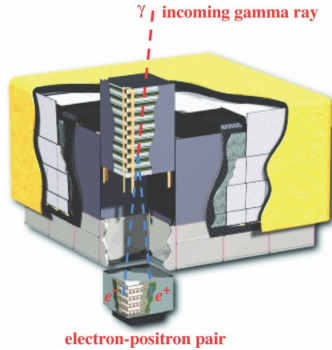


Figure 7: Schematic of the Fermi-LAT with Converter-Tracker, calorimeter and Anticoincidence detector [Atwood et al. 2009]

Figure 7 shows the schematic of the *Fermi*-LAT. The arrangement of the 16 modules can be clearly seen. One module is cut off and shows the Converter-Tracker and the calorimeter. The incoming γ -ray is converted into a e^+e^- pair and the energy is fully absorbed in the calorimeter by the CsI crystal layers. The Anticoincidence detector is shown in yellow.

Atwood et al. 2009 describe the goals of the *Fermi* mission as determining the nature of unidentified sources, investigate the mechanism of particle acceleration (e.g. in AGNs), and using γ -rays for both the indirect search for dark matter as well as to probe the early universe and the cosmic evolution.

3.1.1 Point Spread Function and Instrument Response

The Point Spread Function (PSF) characterizes the ability of the *Fermi*-LAT to reconstruct the arrival direction of the γ -rays. In general, the PSF describes how the imaging system displays a point source, i.e. the area to which a point is mapped. The offset between the real direction \vec{v} and the reconstructed direction \vec{v}' is described by $\delta\vec{v} = |\vec{v} - \vec{v}'|$. The PSF results from the offset,

$$x = \frac{\delta v}{S_p(E)} \quad (10)$$

where $S_p(E)$ describe the characteristic angular size of the PSF as energy dependent scaling function [Ackermann et al. 2013]:

$$S_p(E) = \sqrt{\left[c_0 \cdot \left(\frac{E}{100 \text{MeV}} \right)^{-\beta} \right]^2 + c_1^2} \quad (11)$$

The angular uncertainties result from multiple scattering, where the spatial resolution of the tracker increases for higher energies. The parameter c_0 is the normalization and β sets the scaling with E of the multiple scattering term. c_1 characterizes the instrument-pitch uncertainty. Each event is divided into event types in one of three event class partitions, the "Conversion Type", "PSF Type" or "EDISP Type" partition. The conversion event type indicates whether the event was converted in the front or in the back of the tracker. The PSF and EDISP event types indicate the quality of the reconstruction of the PSF or the energy dispersion E_{disp} in four quality levels each [NASA 2022, ch. 3.2]. The parameters c_0 and c_1 vary for different event types. The distinct values for the calculation of the PSF can be found on the *Fermi* website of NASA 2022 (ch. 5.2).

The Instrument Response function (IRF) indicates the quality of the performance of an measurement. Since the *Fermi*-LAT counts single photon events, the IRF describes the ability to recognize an incoming photon as an event. Furthermore it describes the probability to reconstruct the true γ -ray direction \hat{v}_{true} and energy E_{true} of the photon. The IRF can be factorized into three terms:

$$R = A_{\text{eff}} \times PSF \times D \quad (12)$$

A_{eff} is the effective area of the detector and D the energy dispersion matrix of the photon, which describes the probability distribution to reconstruct a γ -ray energy E' given its true energy E_{true} .

3.2 Imaging Air Cherenkov Telescopes

During the uniform fast motion of a particle in a dielectrical medium, the electromagnetic field of the particle polarizes the medium along the direction of motion. In this process, the atomic-bound electrons in the medium follow the momentum of the passing particle for a brief moment, emitting radiation due to the displacement. If the velocity of the particle in the medium is greater than the phase velocity of the light in the medium, the emitted waves on the wave front are in phase and add constructively. The radiation that results from this is known as Cherenkov radiation (CR) [Jelley 1955]. During the process, the atom is neither excited nor ionized by

the fast moving particle.

Due to Huygens principle the propagation of the radiation occurs at a certain angle θ . Since each atom on the path is a starting point for an elementary wave, the angle depends on the velocity of the moving particle and the composition of the medium.

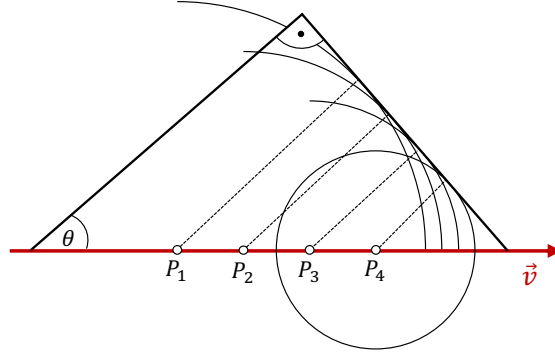


Figure 8: The angle of the Cherenkov radiation is formed by the superposition of the wave fronts created on the line of motion of the astroparticle as it enters the atmosphere.

$$\cos \theta = \frac{1}{\beta n} \quad (13)$$

Figure 8 shows the connection between the velocity \vec{v} of the moving particle and the angle of the CR. The atoms which emit CR are located along the direction of motion. The propagation of the light in the medium is marked as dashed lines and the arising wavefront runs vertically to the propagation of light. By using equation 13, the angle θ can be calculated with the refractive index of the medium n and the velocity ratio $\beta = v/c$.

When arriving at Earth, the high-energy γ rays interact with particles in the atmosphere. In this process, further particles are generated mainly by pair production and bremsstrahlung, which induces a so-called shower. Since the secondary particles have very high energies and thus travel at speed greater than the phase velocity in the atmosphere $v > c/n$, the shower produces CR. The shower usually starts at an altitude of ~ 20 km with e^+e^- pair production. Besides γ radiation, other cosmic rays such as protons can also induce showers. During the interactions, the protons mainly produce pions, which decay further into electrons, muons and photons. Due to the presence of muons and the different form, the shower induced by γ rays can be distinguished from the hadronic shower triggered by protons. The total number of hadronic showers dominates, which is expressed in a suppression factor of up to 10^{-5} for IACTs [Funk 2015].

For a photon energy of 1 TeV the shower reaches its maximum X_{max} at a depth

of ~ 10 km above the ground. The magnitude of the Cherenkov angle in this energy area is 1° or less. This means that the Cherenkov light reaches the ground within a circle of 100 m to 150 m [Hinton and Hofmann 2009]. By catching the light of this secondary products, Imaging Air Cherenkov Telescopes (IACT)

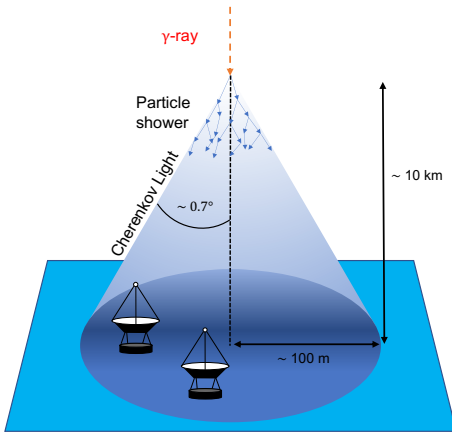


Figure 9: Cherenkov light cone generated at an altitude of ~ 10 km, initiated by a γ -ray, which induces a particle shower when entering the atmosphere.

can observe VHE γ -rays that enter the atmosphere. IACTs turned out to be the most sensitive instrument for pointed observations of γ -ray sources. By setting up an array of telescopes instead of individual IACTs, the observation radius can be drastically increased. All telescopes are connected to a detector that registers the combined signal from the instruments. If the electrical path between the detector and the telescopes is equal, the signal connects in phase. In this case, the angle of the incoming radiation is described by $\theta = \sin^{-1}(N/l_\lambda)$, with N an integer and l_λ as the distance between the telescopes measured in wavelength [Thompson, Moran, and Swenson 2017].

By increasing the distance of the telescopes the resolution of the array can be improved but it must be small enough that all telescopes fit within the Cherenkov light pool [Hinton and Hofmann 2009].

However, the ability to detect certain events is limited. The energy of the photons must be high enough to produce enough Cherenkov light (or energetic enough shower particles). The lower energy limit is called the energy threshold [Funk 2015].

3.2.1 High Energy Stereoscopic System (H.E.S.S.)

H.E.S.S. is a ground-based IACT array that began operations on September 28, 2004. It is located at the Khomas highland in Namibia in the southern hemisphere at an altitude of 1800 a.s.l. [H.E.S.S. Collaboration 2021]. H.E.S.S. initially consisted of 4 telescopes, but was upgraded to 5 telescopes in 2012. In contrast to the four telescopes, the mirror area was increased from 107 m^2 to $\sim 600 \text{ m}^2$ and the focal length from 15 m to 36 m. In the process, it was also possible to reduce the energy threshold from $\sim 100 \text{ GeV}$ to $\sim 30 \text{ GeV}$ [Funk 2015]. This development made the combination of *Fermi* and H.E.S.S. data even easier, providing an important opportunity to study the spectra of extragalactic sources. By adding the fifth Telescope the mission name changed from H.E.S.S. I to H.E.S.S. II. In this work, the data from H.E.S.S. I were used.

4 Analysis Methodology

The following chapter will discuss the methods used for the analysis in this thesis. In addition, there is an overview of the python packages FERMIPY and GAMMAPY, which were used for the analysis of the data.

4.1 Maximum Likelihood Analysis

The *Fermi*-LAT collects data in the form of γ -rays, reconstructing their energy and direction. An important goal is now to use the data to create a model that describes the properties of a given source best. The Maximum likelihood analysis is a method for finding the parameters that best describe the data for a given model. The following explanation is based on the on the NASA [2022](#) website (chapter 7).

The likelihood \mathcal{L} is the probability to obtain fitting data for a given model. The greater the probability, the better the model describes the data. By maximizing the likelihood function, the most appropriate model is found. This is done by varying the model parameters. The input model in this work is a model containing several point-like and diffuse γ -ray sources in the region around the main source. For the maximisation of \mathcal{L} , the spectral parameters of these sources are varied.

The photon counts detected by *Fermi* are binned in three dimensions (3D) containing one spectral (energy) and two spatial information (longitude and latitude). Using this information, the total number of counts can be divided into smaller bins, for example, energy ranges or spatial regions. This means that a small number of counts are grouped into one data point. The number of detected counts within a bin is n_i . The probability of detecting n_i counts in a bin is given by the Poisson distribution $p_i = (m_i^{n_i}/n_i!) e^{-m_i}$, where m_i describes the counts predicted by the model. The likelihood function can now be calculated by multiplying p_i over all i :

$$\mathcal{L} = \prod_i p_i = \prod_i e^{-m_i} \prod_i \frac{m_i^{n_i}}{n_i!} \quad (14)$$

Due to the properties of the exponential function, the product $\prod_i \exp(-m_i)$ can be rewritten as $\exp(-\sum_i m_i)$. As a result the sum over m_i equals the total number of predicted counts N_{pred} . The expression in equation [14](#) is called the *binned likelihood function*, since n_i is finite and can be greater 1. However binning destroys information and by letting the bin size become infinitesimally small, n_i turns either 1 (detected count) or 0 (no count). This leads us to the following expression, namely

the *unbinned likelihood function*:

$$\mathcal{L} = e^{-N_{\text{pred}}} \prod_i m_i \quad (15)$$

Even though the *unbinned* \mathcal{L} theoretically consists of more information, in practice the *binned* analysis is preferred. This method is much less time intensive and for large amounts of data, the loss of information is negligibly small.

Since maximizing $\log \mathcal{L}$ is equal to maximizing \mathcal{L} and the *log-likelihood* is easier to handle, the following equation is commonly used:

$$\log \mathcal{L} = \sum_i \log(m_i^{n_i}/n_i!) - N_{\text{pred}} \quad (16)$$

According to Wilks [1938] two competing statistical models can be compared using the log-likelihood ratio. In doing so, the comparison with the so-called null hypothesis H_0 is used to check whether the hypothesis H_1 is statistically preferred. In the case of the *Fermi* data, the null hypothesis $\mathcal{L}_{max,0}$ is the model without any additional source. $\mathcal{L}_{max,1}$ describes the model with an additional source at specified location. The test statistic TS is defined as,

$$\text{TS} = -2 \log \left(\frac{\mathcal{L}_{max,0}}{\mathcal{L}_{max,1}} \right) \quad (17)$$

with $\lambda = \mathcal{L}_{max,0}/\mathcal{L}_{max,1}$ as log-likelihood ratio. The TS can be used to estimate the presence of a source at a given location. The higher the test statistic, i.e. the more H_1 deviates from H_0 , the more likely it is that a source exists at a particular location. $\sqrt{\text{TS}}$ can approximately be considered as a detection significance.

4.2 PS Analysis Method

The *log-likelihood* is used to find the spectral fitting parameters of the sources within the region of interest (ROI), in which all sources considered in the model are located. From the best-fit model, the predicted number of counts N_{pred} are computed for each pixel. In order to compare the created 3D counts map of the model with those of the data, the residuals of the model has to be investigated. However, this is not straight forward, due to the energy dependence of the PSF, which leads to variations between 3.5° at 100 MeV and $\leq 0.15^\circ$ at >10 GeV in the 68% confinement radius [Atwood et al. 2009]. One method that is mostly used to quantify the agreement of model and data is to create the TS map. In this map, the TS value is calculated for each pixel according to eq. 17 to check if there are additional sources to those of

the model. The higher the TS, the more likely the presence of an additional source at that pixel. The problem with this method is, on the one hand, that it is very computationally intensive and, on the other hand, that it is not sensitive to negative deviations (data<model) [Bruel 2021].

To perform a good data/model comparison for *Fermi*, Bruel 2021 developed the PS³ method. It provides a deviation probability map (PS map) and is sensitive for positive and negative values. It computes the level of deviation between the model and data, by defining the p-value. This describes the probability that the statistical fluctuations of the model reaches at least the level of deviation that corresponds to the deviations of the data. The PS value can then be calculated by the following equation:

$$|\text{PS}| = -\log_{10}(\text{p-value}) \quad (18)$$

The p-value itself can be calculated for each pixel by integrating over the probability density function of the likelihood \mathcal{L} (equation 14). Therefore all counts within the PSF containment radius of 68% are integrated for each energy bin i . If the total number of counts is large enough, the likelihood function can be approximately described by the normal distribution $\mathcal{L} = \sum_i (n_i - m_i)^2 / m_i$, where n_i and m_i are the same variables as in the Poisson distribution. For the sign of the PS value of pixel, the following expression results:

$$\text{sign}(\text{PS}) = \text{sign} \left(\sum_i \frac{n_i - m_i}{\max(1, \sqrt{m_i})} \right) \quad (19)$$

The two equations allow to create a PS map that shows the validity of the model in agreement with the data. Furthermore, they describe whether the deviation is negative (data<model) or positive (data>model).

In summary, the TS map shows whether the model captures all sources in the ROI, while the PS map is an indicator of how good the model fits the data. The python script to create the PS map is available online⁴.

4.3 Spectral Models

Due to the different principles involved in the production of high-energy radiation in AGNs (section 2), a characteristic spectrum is produced over a broad energy range. To understand the processes within a γ -ray source, these spectra are studied. In this context, it is important to consider the flux dN/dE of an extragalactic source,

³The P in PS stands in relation to the p-value and the PSF. Also it is named PS because it sounds similar to TS.

⁴<https://fermi.gsfc.nasa.gov/ssc/data/analysis/user/gtpsmap/gtpsmap.py>

which is described by a specific spectral model. These models depend on various parameters and follow a potential approach. Three different spectral models have been used in this work and are explained in the following.

The first model follows a **Power Law** and is described by the following equation,

$$\frac{dN}{dE} = N_0 \left(\frac{E}{E_0} \right)^{-\Gamma} \quad (20)$$

where N_0 is the amplitude of the Flux, E_0 the reference energy, and Γ the photon index. A similar model is formed by the **Smooth Broken Power Law**, which is described as follows,

$$\frac{dN}{dE} = N_0 \left(\frac{E}{E_0} \right)^{-\gamma_1} \left(1 + \left(\frac{E}{E_b} \right)^{\frac{\gamma_2 - \gamma_1}{\beta}} \right)^{-\beta} \quad (21)$$

with the indices γ_1 , γ_2 and β and E_b as the break value the Flux. The last model that is used to describe the spectrum of PG1553+113 is the **Log Parabola**,

$$\frac{dN}{dE} = N_0 \left(\frac{E}{E_b} \right)^{-(\alpha + \beta \ln(E/E_b))} \quad (22)$$

with $\Gamma_{LP} = -(\alpha + \beta \ln(E/E_0))$ as the photon index. The name of this model is explained by its parabolic shape when the function is plotted in a logarithmic representation ($\log(dN/dE)$ versus $\log(E)$).

One very commonly used method to describe the spectrum of an intergalactic source is to plot the spectral energy distribution (SED). The SED $S(E)$ describes the spectrum, multiplied with E^2 [Lipari 2021]:

$$S(E) = E^2 \left(\frac{dN}{dE} \right) \quad (23)$$

Since Fermi and Hess are sensitive in the region of the second peak of the SED, it is of interest to determine this peak analytically. For this purpose, the first derivative of the SED is set equal to zero. After the calculation according to equation 32 and 33, the logarithmic parabola yields the following peak energy in the SED:

$$E_{\text{peak,LP}} = E_0 e^{\frac{2-\alpha}{2\beta}} \quad (24)$$

For the Smooth Broken Power Law, on the other hand, the energy is as follows:

$$E_{\text{peak,SBPL}} = E_b \left(\frac{2 - \gamma_1}{\gamma_2 - 2} \right)^{\frac{\beta}{\gamma_2 - \gamma_1}} \quad (25)$$

The calculation steps can be found in the appendix under equation [34](#) and [35](#).

4.4 FERMIPY and GAMMAPY Package

The analysis done in this work is based on two different python software packages. The data obtained with *Fermi*-LAT is analysed using FERMIPY, while the combined analysis, including both the data of *Fermi* and H.E.S.S., are analysed in GAMMAPY. Subsequently, a short overview of the two packages is given.

FERMIPY is an open-source python package developed for the analysis of *Fermi*-LAT data. The *Fermitools* (`gt-tools`) [5](#) on which the analysis is based, are primarily written in C++, but can be used via the python interface (`pyLikelihood`). FERMIPY includes other open-source python libraries such as NumPy, SciPy, Matplotlib, and Astropy. The combination of the different libraries allows to perform all necessary mathematical operations and to present the results appropriately. An online documentation about the latest FERMIPY version including tutorials and descriptions of the package is available on their website [6](#).

The first step of the analysis is composing a configuration file, in which various parameters are defined. The settings are explained at the beginning of section [5](#). The analysis of the *Fermi* data is executed within the global analysis state object (GTAnalysis) by using the configuration file as its argument. The analysis begins by using the `setup()` method of the GTAnalysis class. During this process, all important preparatory steps for the analysis are carried out, using the `gt-tools`. The most important tools are summarized in the following based on Wood et al. [2017](#) and NASA [2022](#) (chapter 6 and 7).

First, the data selection is performed, using `gtselect`. Here, only those photons are considered that are suitable for analysis, others are removed. Usually, the data set is selected based on the specified time interval, the energy interval, the chosen ROI, and the maximum zenith angle. The zenith angle is defined as the angle to the direction pointing away from the Earth. Since the Earth's edge begins at a zenith angle of 113° , it is important to define a maximum angle to exclude background events through the Earth. After selecting the events that fulfill the listed criteria,

⁵<https://fermi.gsfc.nasa.gov/ssc/data/analysis/software/>

⁶<https://fermipy.readthedocs.io/en/latest/>

the data is filtered with `gtmktime`. In this step, only those time intervals are chosen in which the data quality is good. Due to e.g. the spacecraft orientation, the data quality can be affected for some periods. The next step is data binning, for which `gtbin` is used. This tool bins the entire event file data, dividing it for example into time, position in the sky (pixel binning), or into different energy bands. The binning of the data is important for several steps in the analysis, e.g. for the creation of count maps, generation of light curves or the calculation of the SED. The livetime quantity describes the time the LAT has observed a source at a given inclination angle. The number of counts detected by this source should therefore depend on the course of Fermi and its angle of incidence. The resulting map of livetimes for all points on the sky is called a livetime cube and can be computed using `gtltcube`. The LAT exposure essentially describes the time spent observing a region on the sky. It indicates with which observation area and over which effective time period the instrument was observing the region. Different angles of incidence change the area of observation, resulting in region-dependent differences in the exposure map, which summarizes the exposure for all points on the sky and can be calculated with `gtexpmap`. It is used to determine the galactic and extragalactic diffuse background. The calculation is made by integrating the IRF (see section [3.1.1](#)) over the energy E and direction \hat{v} of the photons collected within the ROI.

$$\epsilon(E, \hat{v}) = \int_{\text{ROI}} R(E, \hat{v}) dE d\hat{v} \quad (26)$$

Predicted counts of a given source i can then be calculated by integrating the exposure,

$$N_{\text{pred}} = \int \epsilon(E, \hat{v}) F_i(E, \hat{v}) dE d\hat{v} \quad (27)$$

and the intensity F_i (energy flux) of the source.

The tool `gtsrcmaps` calculates the model count maps. This type of map includes all sources and is scaled by the exposure and folded with the PSF. A very important tool is also `gtlike`, which is used to perform both binned and unbinned likelihood calculations. For these calculations, many of the previous tools are crucial. In particular, the exposure and counts map are important for the binned likelihood, the livetime cube and the source maps. `gtlike` calculates the TS values and the spectral parameters (power law or log parabola) of each source.

After the data has been prepared, it can be examined using further useful analysis methods of GTAnalysis [Wood et al. [2017](#)].

GAMMAPY is also an open-source Python package primarily aimed at analyzing data from imaging air Cherenkov telescopes. It can be used to analyse data from

different instruments, given the IRF's. Currently, GAMMAPY is used, for example, for the analysis of *Fermi* and H.E.S.S. data, but also for Cherenkov Telescope Array (CTA) simulations. Just like FERMIPY, the GAMMAPY package is based on other Python packages, notably Astropy and NumPy. Other optional packages are Scipy and Sherpa.

The analysis tools consist of different methods such as temporal computations of light curves, performing one-dimensional or three-dimensional spectral analysis of one spectral and two spatial dimensions, estimations of the γ -ray background, as well as creating sky maps (e.g. signal, background, etc) [Deil et al. 2017]. Further analysis options and tutorials of GAMMAPY can be found on their website⁷.

Overall, especially with respect to CTA, GAMMAPY is an essential tool for anyone working in the field of gamma-ray astronomy. The analysis in this work is performed with version 1.0.

5 Analysis

In the following section, the analysis of the 2019 observed data from PG 1553+113 is discussed. Section 5.1 evaluates the data measured with *Fermi*-LAT in 2019. Section 5.2 discusses the results of a combined fit using GAMMAPY, in which both the data measured with *Fermi*-LAT and the data measured with the H.E.S.S. telescope are jointly fit. The time period of the data is adjusted to the γ -ray flare between April and May 2019 observed with H.E.S.S.

5.1 Fermi Data Analysis with FERMIPY

As discussed in section 3.1, the *Fermi*-LAT is constantly orbiting the Earth. The fact that every source can be seen every three hours for approximately 30 minutes allows one to measure a large fraction of the flux of extragalactic sources over a long period of time. In order to derive the average flux over a long period of time, including the H.E.S.S. observation window, the period was set from January 1, 2019 to December 31, 2019 for the first steps of the analysis. By using these settings the flux of the γ -ray flare can be compared with data from a longer time scale. Beginning with the analysis in section 5.2, the period is adjusted to April 8 until May 10. This adaption includes most of the H.E.S.S. data from the γ -ray flare in 2019 (analysis in bachelor's thesis by Abed 2022).

⁷<https://gammapy.org>

5.1.1 Setup

The analysis is performed with the LAT Fermitools (version 2.2.0) by using the python package FERMIPY. The `P8R3_SOURCE_V3` is set as the instrument's response function. This class distinguishes between 8 different PSF event types and is used for the analysis of point sources and moderately extended sources, which makes it appropriate for the analysis in this work [NASA 2022, chapter 3.2].

For the analysis of the *Fermi* data, all sources within a square region of $15^\circ \times 15^\circ$ (centred on the location of PG1553+113) are selected for inclusion in the model. However, only those photons that were detected within the region of interest (square area of $10^\circ \times 10^\circ$) are assigned to each point source. The energy range of the selected photons is 100 MeV - 316 GeV. In addition to the model list of sources within the square region, the Galactic and isotropic backgrounds have been added. The Galactic Background takes into account the interstellar diffuse γ -ray emission from the Milky Way [Soheila et al. 2023]. For this component, the spatial and spectral template `gll_iem_v07.fits`⁸ is used. The spectral template `iso_P8R3_SOURCE_V3_v1.txt` was used for the isotropic background. The configuration file in which all settings are defined for the analysis can be found in the appendix, see figure 20. The energy range and the ROI will be adjusted for the GAMMAPY analysis.

According to the explanation in section 4.4 the set up of the data was performed by using the `gt-tools`. In this process, among other things, the exposure map and the counts cube were created. Furthermore, the PSF and the detector response matrix D (energy dispersion) were generated, which is crucial for the later analysis in GAMMAPY.

Two counts maps are shown in figure 10 for the whole *Fermi* data in 2019 and within the ROI. The counts in the left map are reconstructed from the data; those in the right map are estimated by the model. It can be seen that the model represents the data quite well. Still, slight differences are recognizable, namely that the counts map based on the data has sharper edges, whereas the map created by the model looks smeared.

As described in section 4.2, the agreement of the data and model can be estimated in two different ways. The left diagram in figure 11 shows the $\sqrt{\text{TS}}$ map, which provides information whether all sources in the ROI are described by the model. One can see a hand full of spots in the outer part of the diagram, where the $\sqrt{\text{TS}}$ value is relatively high ($\sqrt{\text{TS}} > 3\sigma$). At these locations, additional sources could be present, due to the deviation of the model. The PS map is shown on the right

⁸<https://fermi.gsfc.nasa.gov/ssc/data/access/lat/BackgroundModels.html>

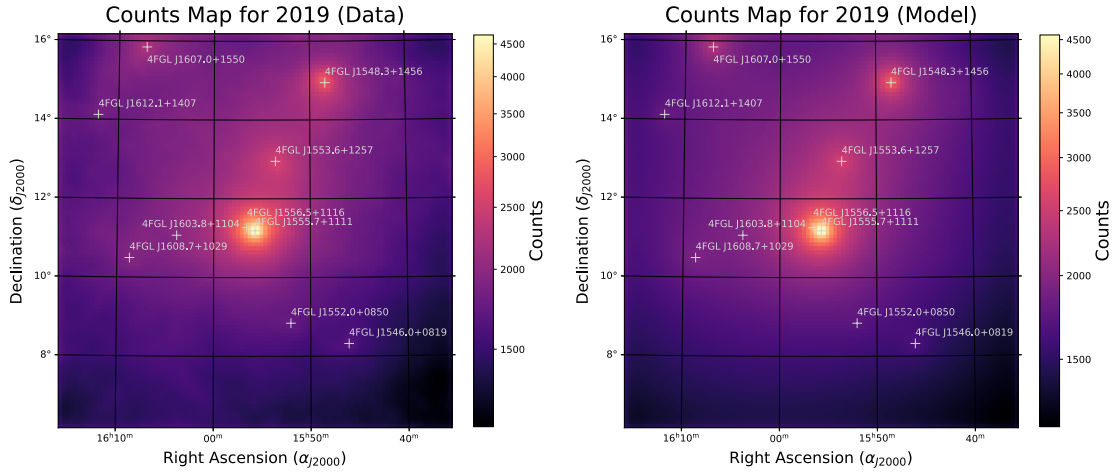


Figure 10: Counts maps of the ROI for 2019 based on the *Fermi* observations. **Left:** Counts map based on the reconstruction of the data. **Right:** Counts map created on the basis of the model.

sight of the figure. It can be observed, that all locations with a high $\sqrt{\text{TS}}$ value correspond to locations with a high value on the PS map. In addition, more bright spots can be seen on the PS map, especially in the lower right corner. Moreover, the map shows negative PS values that describe negative deviations of the model. These dark spots illustrate directions where the model suggests too many counts compared to the data. The dark spots that are right next to the light spots in the lower right corner of the PS map could be an explanation for the fact that such a deviation is not visible in the $\sqrt{\text{TS}}$ map. The deviations cancel each other out, so to speak, which means that significant deviations in the $\sqrt{\text{TS}}$ map are not detected.

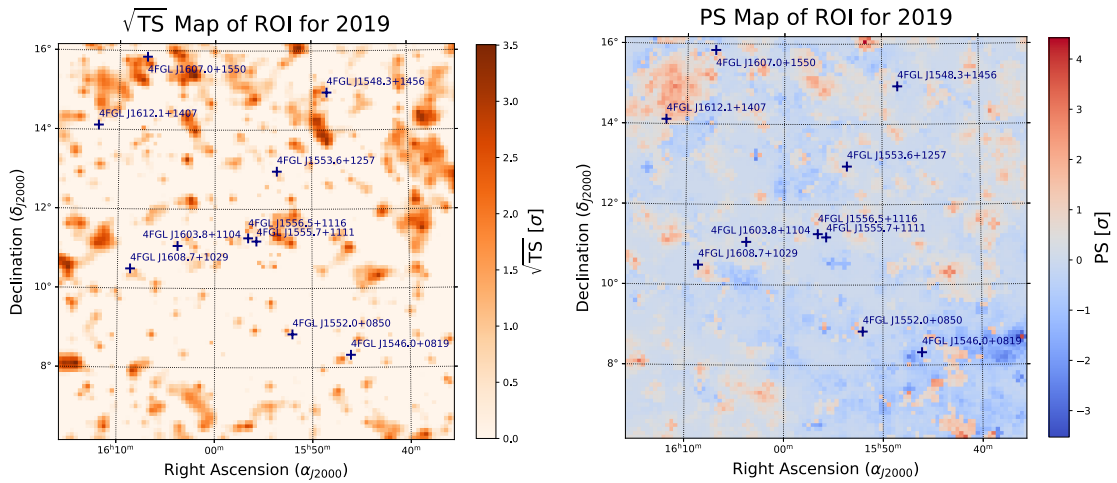


Figure 11: $\sqrt{\text{TS}}$ and PS map of ROI for 2019.

However, in total one can say that both the $\sqrt{\text{TS}}$ and the PS map shows that the

model fits the data quite well. Large deviations above 5σ are not present, which means that all relevant sources are described by the model.

5.1.2 Spectral Energy Distribution

The SED is a method for analyzing the spectral properties of sources. Different spectral models are suggested to describe the spectrum of a source the best. According to Abed [2022], the model that fits best to the VHE spectrum of PG 1553+113 turns out to be the Log Parabola, see eq. [22]. In this section the spectrum of the HE data measured with *Fermi*-LAT is to be discussed.

The settings described at the beginning of the chapter were used to create the SED. In addition to the setup that was performed before, the relevant sources for the analysis must be selected as preparation for the SED calculation. For the following fit, the normalization and the shape of all sources are left free to vary, when they have a test statistic of $TS > 4$, the predicted counts are $N_{\text{pred}} > 10$, and the source is located within a radius of 10° . Furthermore, the galactic and isotropic background were included in the fit. After finishing the settings, the SED as well as the best fit of the spectral model were created.

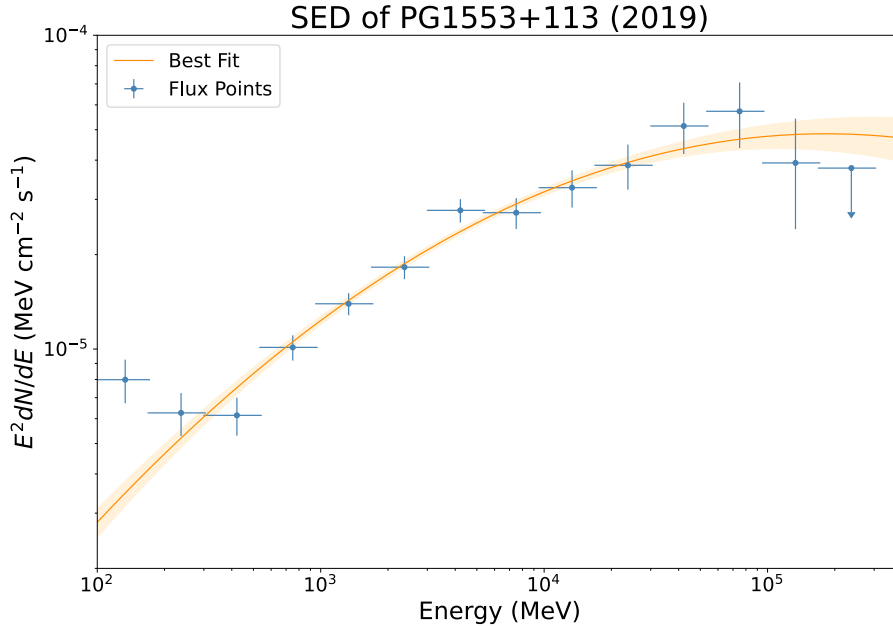


Figure 12: Average SED of PG1553+113 in 2019 based on *Fermi* data. The best fit and the calculated flux points are shown

Figure [12] shows the SED of PG 1553+113 in 2019. The SED is plotted as spectral model normalized by E^2 against the Energy E . The scales of the axes are logarithmic and the energy is divided into four bins per magnitude. Each flux point contains

the data within one energy bin. The data points with a test statistic of $TS < 4$ are plotted as upper limits (indicated as an arrow pointing downward). The figure, also shows the best fit of the SED calculation.

The best fit parameters are estimated to $N_0 = (1.574 \pm 0.072) \times 10^{-12} \text{ MeV}^{-1} \text{ cm}^{-2} \text{ s}^{-1}$, $\alpha = 1.608 \pm 0.025$, $\beta = (5.056 \pm 1.357) \times 10^{-2}$ and $E_b = 3.802 \text{ GeV}$. The data of the estimated flux points can be found in table 3.

It can be seen that the flux points follow the shape of the SED based on the Log Parabola as spectral model quite well. Most points lie within the 1σ confidence interval of the fit. Especially in the energy range between 500 MeV - 100 GeV the variance is small. For both smaller and higher energies, the deviation of the flux points increases. On the one hand, one possible reason for that could be the increasing PSF and decreasing effective area for low-energetic photons. On the other hand, it might be due to the effect of the EBL absorption, which was not considered in the SED. The absorption starts at energies of $E_\gamma > 10 \text{ GeV}$ and could therefore have caused some of the deviation of the flux points at higher energies.

5.1.3 Light Curves

Light curves describe the variation of the photon flux emitted from a source over time. Here, the measured flux in a specific energy range is plotted against time. This form of visualisation can be used to show the activity of γ -ray sources over a long period of time.

The calculation of the flux points is done by integrating the spectral flux over the energy range that was observed. For estimating the light curves the Power Law was used as the spectral model. According to equation 20, the flux within the energy range ΔE can be described in the following form:

$$\frac{dN}{dE \Delta E} = \int_{\Delta E} \frac{dN}{dE} dE = \int_{\Delta E} N_0 \left(\frac{E}{E_0} \right)^{-\Gamma} dE \quad (28)$$

The data points of the light curve are characterized by their temporal binning, which summarizes a period of data. Each of these bins contains the data of detected photons for that time interval. By analyzing all photon counts, the best fit of the spectral model can be calculated for a single bin using FERMIPY. The `lightcurve` method was used to perform an end-to-end analysis of the data for each time interval. During the calculation of the light curve, both the index and the reference energy were fixed. The values are calculated as the best fit of the spectral analysis.

⁹<https://fermipy.readthedocs.io/en/latest/advanced/lightcurve.html>

Thus, only the amplitude N_0 is varied, the index and reference energy are fixed at $\Gamma = -1.655$ and $E_0 = 3.802$ GeV.

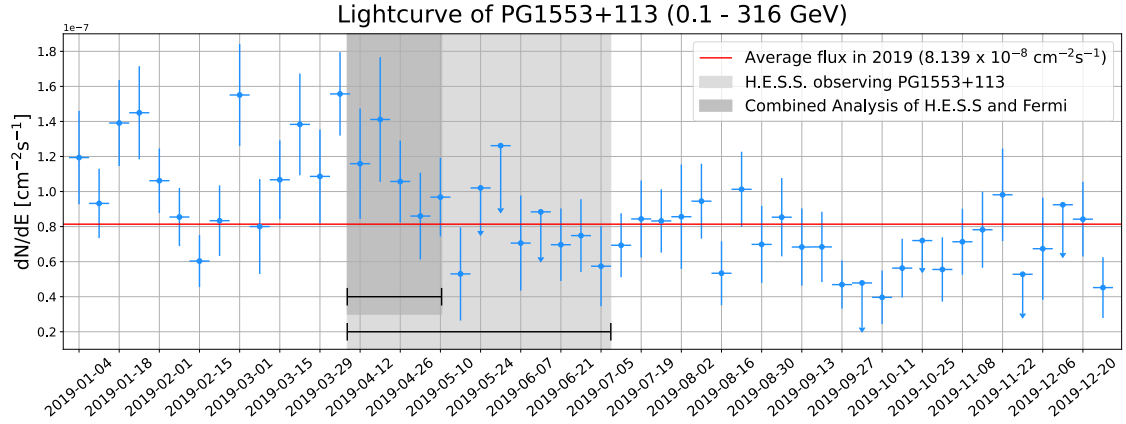


Figure 13: Light curve of PG 1553+113 in 2019. Photons within the energy range 100 MeV - 316 GeV were selected and the time binning is one week. The spectral model is a Power Law.

Figure 13 shows the light curve of PG 1553+113 in 2019, selecting photons with energies ranging from 100 MeV to 316 GeV. The size of each time bin is one week. Data with a test statistic $TS < 4$ are shown as upper limits. In addition, the time intervals of the H.E.S.S. observations and the combined analysis (section 5.2) are highlighted in the figure.

The light curve shows the variability of PG 1553+113 quite well. The photon flux fluctuates between minima and maxima in a few weeks. At the beginning of 2019, a large flux can be recognized. Especially in January, March and April the data points are above average (see figure). The maximum of its activity is reached by the blazar with a value of $(1.557 \pm 0.238) \times 10^{-7} \text{ cm}^{-2} \text{ s}^{-1}$ in the first week of April. At the same time H.E.S.S. began its observations on the blazar.

Bayesian Blocks

As shown in the light curve of PG 1553+113, flares of blazars are not predictable. The variability of AGNs can have various shapes that change in short periods of time. These variations can occur randomly, periodically or in any other unknown form, usually following a coloured noise spectrum, see section 2.3.1. To study the activity of extragalactic sources, Jeffrey D. Scargle developed the Bayesian Blocks algorithm in 1998 as a statistical method [Scargle 1998]. In this context, the flux points are statistically evaluated using the maximum log-likelihood method and new time bins are created on the basis of this evaluation. For this purpose, the maximum of the log-likelihood function is used as fitness function for point measurements according

to Scargle et al. [2013]:

$$\log \mathcal{L}_{max}^{(k)} = \frac{b_k^2}{4a_k} \quad (29)$$

The quantities a_k and b_k depend on the data points x_n and its error σ_n and are determined as follows:

$$a_k = \frac{1}{2} \sum_n \frac{1}{\sigma_n^2} \quad (30)$$

$$b_k = - \sum_n \frac{x_n}{\sigma_n^2} \quad (31)$$

The bins of the Bayesian Blocks in figure [14] were estimated with the `bayesian_blocks` function of the `astropy.stats` package [10]. Therefore, all flux points in figure [13] and its errors were inserted in the function as well as the weekly time bins. By setting the parameter `fitness = "measure"`, the point measurement fitness function were used, assuming a Gaussian statistic. After calculating the new bins as intervals of time, the light curve of the Bayesian Blocks was created according to the weekly light curve.

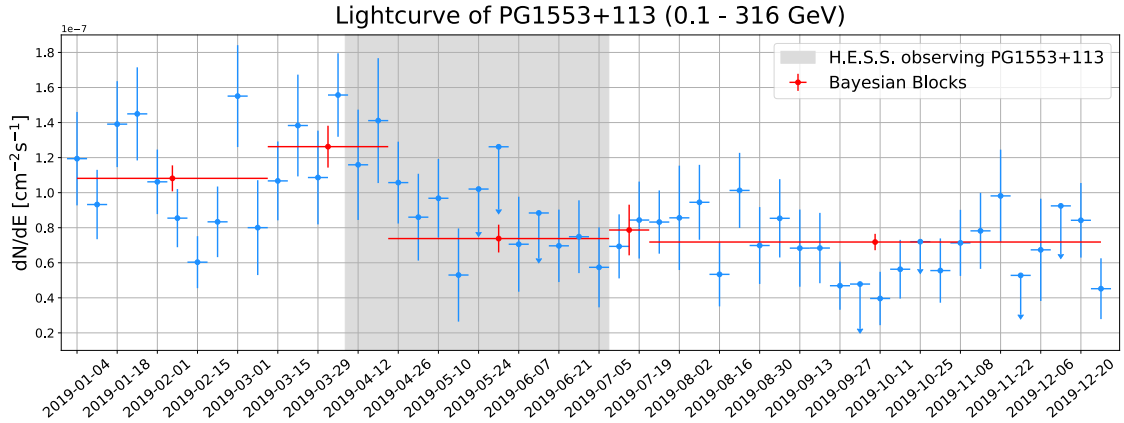


Figure 14: Light curve of PG 1553+113 in 2019 with Bayesian Blocks.

Figure [14] shows the light curve of PG 1553+113, where the flux points are plotted with both weekly binning and the bin size created by the Bayesian block algorithm. The period in which H.E.S.S. was observing the source is additionally highlighted in this diagram again.

We see that the bins created with Bayesian Blocks algorithm follow the course of the weekly bins. A high flux of photons can be recognized from January to April 2019, in which the maximum is seen in March and April. In the end of April the flux decreases to an almost constant level until the end of the year. Looking at the period of H.E.S.S. observations, one can see a division of Bayesian blocks into two bins.

¹⁰https://docs.astropy.org/en/stable/api/astropy.stats.bayesian_blocks.html

The time of the transition point is April 23. The variation of the flux seems to fit to those of higher energies. In Abed [2022](#), the nightly light curve of PG 1553+113 was discussed for the period of the H.E.S.S. observations. For the creation of the light curve, events in the energy range between (0.26 - 1.62) TeV were selected. Again, the Bayesian block algorithm was performed, which calculated a transition point at April 24.

5.2 Fermi and H.E.S.S. Data Analysis with GAMMAPY

The following section discusses the capabilities of GAMMAPY to process data from multiple instruments. In the first part, the analysis of the data collected by *Fermi* is repeated with GAMMAPY and compared with the analysis of FERMIPY. In this step, the time period is changed to the H.E.S.S. observations. In the second part, the analysis of the H.E.S.S. data is discussed before all data is summarized in a joint fit in the last step.

5.2.1 Fermi Analysis

In this section, the *Fermi*-LAT spectrum is analysed using GAMMAPY. The minimum energy is changed to $E_{min} = 1$ GeV, because the discrepancies between the flux points and the best fit are too large for small energies. In addition, GAMMAPY cannot handle the large PSF below 1 GeV. To enable the processing of *Fermi* data in GAMMAPY, some important information must be taken from FERMIPY. For this purpose, the needed files are created according to the description in section [5.1.1](#) after the setup has been performed. However, some adjustments regarding the settings have to be made for this step. Since the FERMIPY analysis includes sources that are outside of the ROI but extend into it, due to the angular resolution, the ROI for the GAMMAPY analysis must be adjusted to $15^\circ \times 15^\circ$. Because of energy dispersion, some events with lower or higher energy are reconstructed within the energy range. In contrast to GAMMAPY, the FERMIPY analysis is adding one energy bin above and below this range. For this reason, the energy range must also be changed and is set to $562 \text{ MeV} < E < 562 \text{ GeV}$, which corresponds to one more bin each side (four bins per decade in logarithmic scale) [Unbehau [2020](#)].

The analysis via GAMMAPY is based on creating `datasets()` [\[11\]](#). All important information is stored within this object by reading the created files and passing them to the dataset. The object used for the *Fermi* analysis is the `MapDataset()`, which contains the counts cube, the exposure of the ROI, the PSF as well as the DRM (en-

¹¹<https://docs.gammapy.org/dev/api-reference/datasets.html>

ergy dispersion) as information. The corresponding files were read in as maps and passed to the dataset in the correct shape. In addition, the model map of the point sources was read in, supplemented by the galactic and isotropic diffuse background. Since the ROI was increased for the GAMMAPY analysis, an additional mask must be defined, that restricts the region to that used in the FERMIPY analysis ($10^\circ \times 10^\circ$) and also adjusts the energy range to $1 \text{ GeV} < E < 316 \text{ GeV}$.

Due to the fact that all necessary files are read in and passed to the dataset, no information nor statistics are lost. The analysis starts by computing the parameters of the best fit via the maximum likelihood method. Since in the following evaluation the data of H.E.S.S. and *Fermi* are to be combined, the detection period is already adjusted in this step to the H.E.S.S. observations of PG1553+113. The values that result for the spectral analysis in GAMMAPY are $N_0 = (2.237 \pm 0.324) \times 10^{-12} \text{ MeV}^{-1} \text{ cm}^{-2} \text{ s}^{-1}$, $\alpha = 1.624 \pm 0.155$, $\beta = (4.509 \pm 7.018) \times 10^{-2}$ and $E_b = 3.802 \text{ GeV}$.

The estimation of the flux points for the spectral model is done in a separate step, by using the `FluxPointsEstimator()` as a method of the estimators package [\[12\]](#). After defining the energy edges of the bins, the flux points are created based on the data set.

Figure [\[15\]](#) shows the result of the SED analysis in GAMMAPY compared to the SED created by FERMIPY. Due to the shorter time period, less data was used for the analysis than in figure [\[12\]](#), which is reflected in larger deviations between the best fit and the flux points, although all flux points still lie within the confidence interval of the best fit. However, it can be seen that the flux points and best fit calculated by GAMMAPY agree very well with those of the FERMIPY analysis. This can also be verified by the best fit parameters $N_0 = (2.347 \pm 0.326) \times 10^{-12} \text{ MeV}^{-1} \text{ cm}^{-2} \text{ s}^{-1}$, $\alpha = 1.637 \pm 0.147$, $\beta = (3.904 \pm 6.726) \times 10^{-2}$ and $E_b = 3.802 \text{ GeV}$ of the FERMIPY analysis. These are very close to those listed above. The data of the flux points in this plot can be found in tables [\[4\]](#), [\[5\]](#).

The similar results are a consequence of using all the data from FERMIPY and show that GAMMAPY uses the full statistics for the analysis. In the following sections, this functionality is further used in the combined analysis.

5.2.2 H.E.S.S. Analysis

Since H.E.S.S. data is not public, the data used in this work was provided by Manuel Meyer's research group. Similar to the processing of the *Fermi* events, datasets are also created in GAMMAPY for the H.E.S.S. data. Due to the fact that H.E.S.S.

¹²<https://docs.gammapy.org/dev/api-reference/estimators.html>

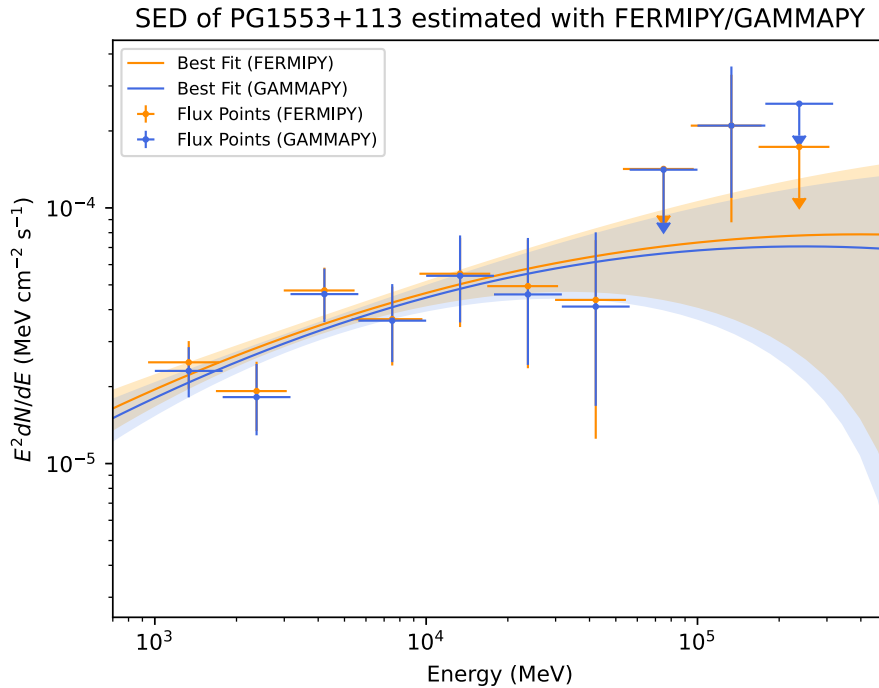


Figure 15: The SED of PG1553+113 for the period of H.E.S.S. observations. The best fit and the flux points were calculated once with GAMMAPY and FERMIPY.

is a ground-based telescope array, the entire sky cannot be observed permanently, but the system collects data from specific regions of the sky in so-called runs. Each run of the H.E.S.S. telescopes covers an observation time of approximately 28 minutes and includes all detected events within this period [Abramowski et al. 2015]. The specific observation of certain sky regions is the reason why the observation of PG1553+113 was done by H.E.S.S. for only a limited period of time.

For the analysis, all usable runs are collected and stored within one dataset. The chosen model is the Log Parabola with EBL absorption (see equation 9), since the reconstructed γ -ray events lie within an energy range that is affected by the EBL. The absorption is given by $\exp(-\tau_{\gamma\gamma}(z, E))$, which is calculated using the `tau_from_model()` method of the `ebtable`¹³ package. The redshift used for the calculation was determined by Dorigo Jones et al. 2022 using the highest absorption line of the Lyman-alpha ($\text{Ly-}\alpha$) series. This line lies at the upper edge of the Ly- α forest, in the UV region. Using this method, the redshift of PG1553+113 was found to be $z=0.433$. The EBL model is calculated using the optical depth $\tau_{\gamma\gamma}(z, E)$ according to Dominguez et al. 2011.

After creating the spectral model including the EBL, the fit of the model is per-

¹³<https://github.com/me-manu/ebtable>

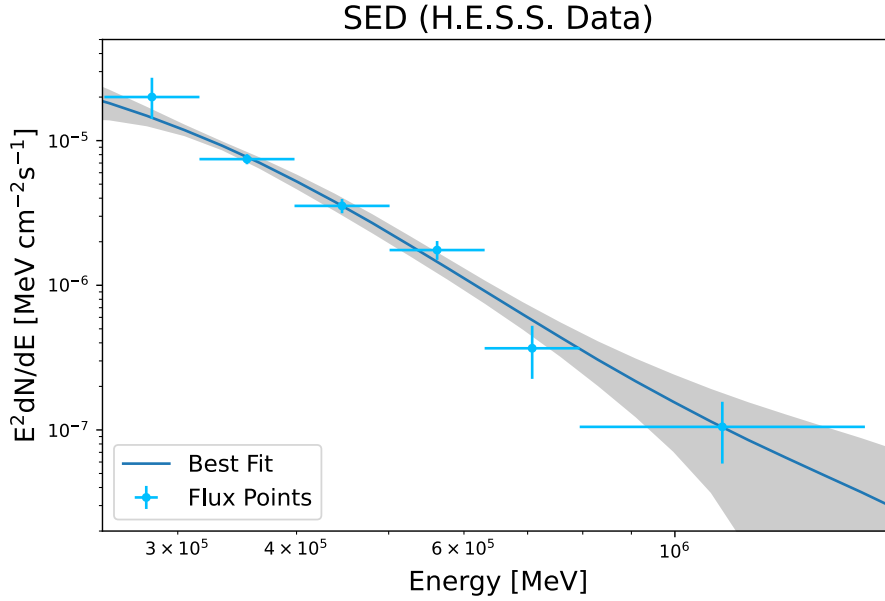


Figure 16: SED of PG1553+113 using H.E.S.S. data.

formed. This is followed by the calculation of the flux points as described in the previous section. As in Abed [2022](#), only bins with an excess of events compared to the background of $N > 3$ were considered. Due to the small number of counts at high energies, the last four bins are combined into one, so that enough events are evaluated in this energy interval. The data of the estimated flux points can be found in table [6](#).

Figure [16](#) shows the SED of PG1553+113 for the period of H.E.S.S. observations, including the flux points and the best fit of the analysis. The best fit parameters are $N_0 = (1.257 \pm 0.858) \times 10^{-16} \text{ MeV}^{-1} \text{ cm}^{-2} \text{ s}^{-1}$, $\alpha = 2.263 \pm 0.658$, $\beta = (1.32 \pm 9.11) \times 10^{-1}$ and $E_b = (6.251 \pm 1.893) \times 10^2 \text{ GeV}$. It can be seen that all flux points are within or at the limit of the confidence interval of the fit. Since the statistics are smaller for higher energies, the confidence interval shows an increasing deviation for high energies. On the one hand, this is reflected in the errors, especially β 's, which predominates for large energies. On the other hand, the E^2 scaling causes larger deviations for increasingly high energies. Also, at small energies the deviation increases. In this region, the error of the amplitude dominates.

5.2.3 Combined Analysis of Fermi and H.E.S.S. Data

The two fits and flux points created in the previous sections are combined in figure [17](#). The plot suggests the form of a combined analysis. However, large differences can be seen, especially in the transitional energy range, where flux points have been recorded and calculated with both instruments. The best fit of the *Fermi* data lies

above the other and does not show any curvature in the direction of the H.E.S.S. flux points.

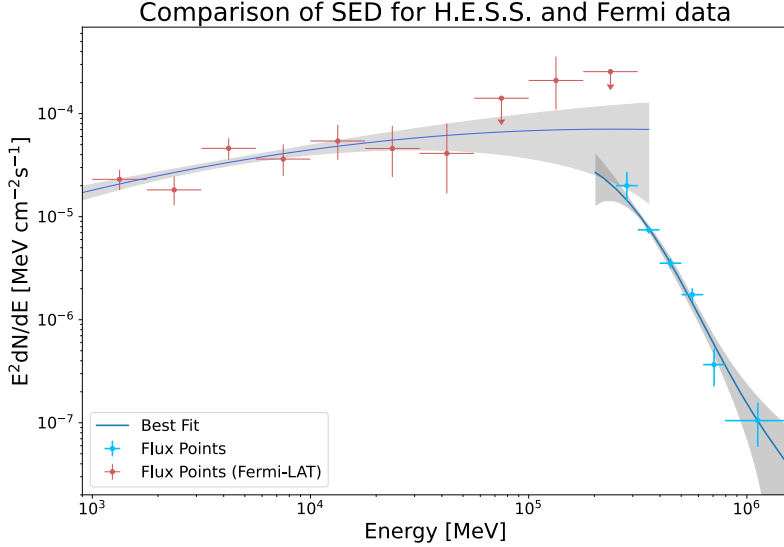


Figure 17: Combined illustration of the previous two SEDs. The best fit and the flux points are plotted for the H.E.S.S. and the *Fermi* data

After fitting both parts of the spectrum of PG1553+113 it's time to combine the data in a joint fit. For this purpose the two datasets are merged, so that the entire statistics can be used for further analysis. Therefore, the point source models of FERMIPY analysis are used and EBL absorption is added to the main source spectral model. The fitting is done first with the Log Parabola and then with the Smooth Broken Power Law (see eq. [21](#)) as an alternative to determine which of the spectral models best describes the overall source flux. During the analysis, the spectral parameters of the main source and the parameters of the diffuse background were free to vary. In total, there were eight free parameters in both models.

Figure [18](#) shows the combined fit with the Log Parabola as the spectral model. As this model has already been used for the previous analyses, it makes sense to start with it to create the combined fit. The best parameters of the analysis are calculated to $N_0 = (9.999 \pm 0.097) \times 10^{-11} \text{ MeV}^{-1} \text{ cm}^{-2} \text{ s}^{-1}$, $\alpha = (2.866 \pm 3.567) \times 10^{-2}$, $\beta = (1.195 \pm 0.049) \times 10^{-1}$ and $E_0 = (1.5428 \pm 0.0321) \times 10^{-1} \text{ GeV}$.

As described above, the emission in this energy range is predominantly produced by IC scattering and π^0 decay. The graph illustrates the resulting second peak of the SED over a large range. Only by merging the two data sets, a joint fit for a larger range of the peak is possible. According to equation [24](#), the peak of the SED can be calculated using the best fit parameters. This results in a value of $E_{\text{peak,LP}} = (5.8951 \pm 2.5076) \times 10^1 \text{ GeV}$.

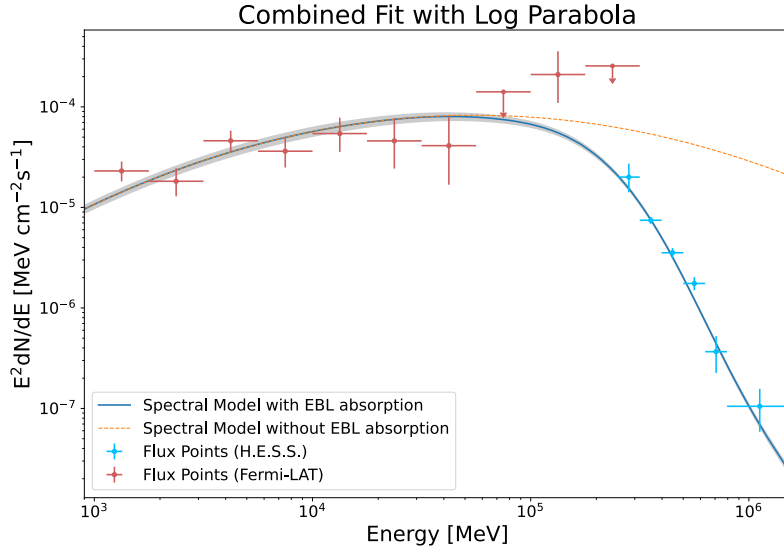


Figure 18: Joint fit of the H.E.S.S. and the *Fermi* data. The spectral model is a logarithmic parabola. Besides the flux points and the best fit assuming EBL absorption, the intrinsic spectrum without EBL absorption is also shown.

It can be seen, that the flux points are relatively well described by the best fit. However, the function is forced to drop strongly after the *Fermi* data. Due to EBL absorption, the values of the H.E.S.S. flux points suddenly fall severely below the energy peak. The red flux points in the high energy region lie above the best fit. This is due to the previously mentioned EBL absorption, but also, and particularly, because of a lack of data that result in a small statistic. Due to the parabolic shape of the fit, other flux points are not described as well as before by the function, either. This is especially true for the data measured by *Fermi*, but larger deviations can also be seen in the blue flux points.

A possibility to estimate the goodness of the fit is by performing the χ^2 test. This checks how well the data fits the model by comparing each flux point with the fit's corresponding data point. Using the sum $\chi^2 = \sum_i (O_i - C_i)^2 / \sigma_i^2$, this value can be determined, with O_i the observations (flux points) with its significance σ_i and C_i the data points of the fit. The goal is for χ^2 to be as small as possible, so that the model is very close to the data. However, if the value is too small, the model may be too complex or the flux point errors may be overestimated. Mostly, the reduced χ^2 is given, where $\chi^2/d.o.f.$ is normalised by the so-called degrees of freedom (d.o.f.). A value of $\chi^2/d.o.f. = 1$ essentially expresses a very good value [Andrae, Schulze-Hartung, and Melchior 2010]. The fit shown above results in a value of $\chi^2/d.o.f. = 7.869$ for the Log Parabola.

In contrast, figure 19 illustrates the combined fit using the Smoothed Broken Power Law. It can be seen that this fit describes the flux points of H.E.S.S. much better than the Log Parabola. Also the function follows the position of the *Fermi* data points very closely, so that almost all points, except those at higher energies, lie very close within the confidence interval. The calculated parameters for the spectral model are $N_0 = (6.877 \pm 4.761) \times 10^{-15} \text{ MeV}^{-1} \text{ cm}^{-2} \text{ s}^{-1}$, $\gamma_1 = 1.243 \pm 0.124$, $\gamma_2 = 2.725 \pm 0.281$, $\beta = 4$, $E_0 = 1 \text{ TeV}$ and $E_b = (7.807 \pm 5.505) \times 10^1 \text{ GeV}$. The index β and the reference energy E_0 were fixed during the calculation. According to equation 25, the values of the parameters result in an SED peak at $E_{\text{peak,LP}} = (8.7723 \pm 10.1308) \times 10^1 \text{ GeV}$.

Even though most of the flux points are better represented by the Smooth Broken Power Law, the $\chi^2/d.o.f$ value is with 8.304 slightly higher than that of the Log Parabola. This fit does not fit the data as well as the one before. However, as mentioned, the data of the three most energetic *Fermi* flux points are very different. In the resulting value, these three flux points take the largest percentage. In order to improve the statistic, and thus make a more accurate statement about the validity of the model, more data would have to be included for this energy range.

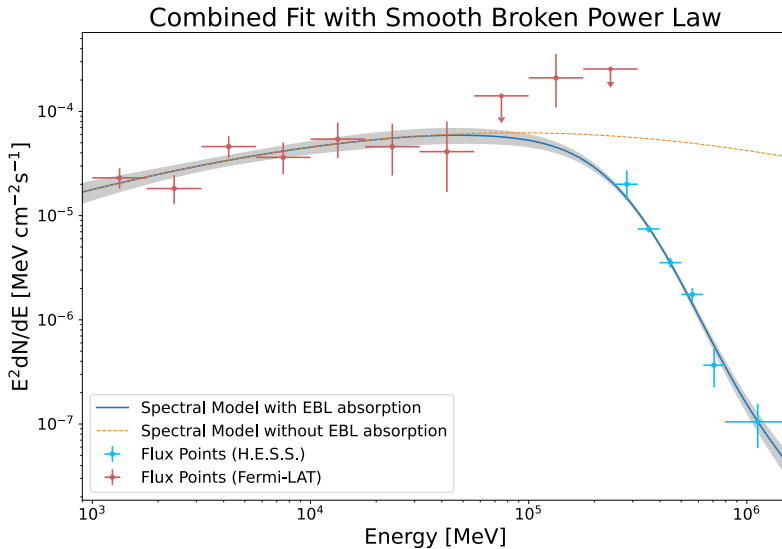


Figure 19: Joint fit of the H.E.S.S. and the *Fermi* data. The spectral model is a smooth broken power law. Besides the flux points and the best fit assuming EBL absorption, the intrinsic spectrum without EBL absorption is also shown.

Additionally to the best fit, both figures show the spectral model without the absorption of the EBL. This function illustrates the shape of the intrinsic spectrum emitted by the source. The strong deviation from the observed spectrum clearly shows the strong effect of EBL absorption on the emitted γ -rays for high energies.

Interestingly, the attenuation by the EBL already begins at energies at which *Fermi* is still sensitive. It does show that considering the EBL, as a source of opacity, could be appropriate for higher energies in the *Fermi* analysis. Besides, there are other reasons for the deviations in this final analysis. One very important issue is the amount of data used for the fit. Unfortunately the observations of PG1553+113 are limited to those periods in which the H.E.S.S. telescope was observing the corresponding region in the sky. The interval used for the combined analysis in this work had a length of only 32 days. As a result, the deviations of the flux points are significantly larger, compared to the SED for the whole year 2019 (figure 12). If instead more data would be used over a longer period of time, the joint analysis would produce better results and errors could be minimized.

In summary, it can be concluded that the combined fit worked out really well in GAMMAPY. By creating a dataset it is very easy to merge the observations of two different instruments. The advantage here is that by reading in all the needed files (counts maps, exposure maps, models map, etc.), no information is lost during this process and the whole statistic is used for the analysis. While the Log Parabola describes the two measurements very well individually, the Smooth Broken Power Law seems to fit better to the flux points of the combined analysis. The generated images thus describe a broad spectrum of the emission caused by PG1553+113, which also shows the maximum of the second peak of the SED.

6 Conclusion

This thesis examined the combined data set of *Fermi* and H.E.S.S. regarding the blazar PG1553+113. In order to find the best fit, multiple analytical tools were used. This section summarises the steps and results of the analysis and provides a contextual outlook for future work in this field.

The first part of the analysis was performed by the Python package FERMIPY. The Fermitools represent a good and easy way of evaluating extragalactic γ -ray sources based on a binned maximum likelihood analysis. The TS map is a commonly used method to determine whether a model represents all sources in the ROI. However, this method cannot estimate the validity of a source because the TS value only shows positive deviations. A possibility to assess the agreement between model and data is given by the PS map, which takes the energy-dependent resolution into account, based on the PSF. It responds to both negative and positive differences and has been shown to identify discrepancies between the model and the data to which the TS map is blind. With the help of the two methods, a model was created on the

basis of which the spectral analysis of PG 1553+113 was performed afterwards. The SED was firstly estimated for the full year of 2019, considering the Log Parabola as spectral model, due to the results of Abed [2022](#). The HE flux points followed the shape of the model comparable to that calculated from the H.E.S.S. data. Nevertheless, the deviations increased at low and high energies. On the one hand, this can be explained by the energy-dependent PSF, on the other hand the detected events in the high energy range could already be affected by EBL absorption. The photon index was estimated to $\Gamma_{LP} = 1.608 \pm 0.025$ at the reference energy $E_0 = 3.802$ GeV.

The second part of the spectral analysis was continued via GAMMAPY. The focus here was to create a joint fit using both the data of H.E.S.S. and *Fermi*. A comparison with FERMIPY showed that very similar results were obtained when calculating the SED. Subsequently, the data from both instruments merged in a joint fit. This allowed the entire peak in the energy range to be shown for the first time. By using the best fit parameters, this thesis was able to calculate the maximum energy of the peak's intrinsic spectrum.

The fit with the Log Parabola showed a stronger deviation to most data points than the Smooth Broken Power Law. However, the $\chi^2/d.o.f.$ value shows that the Log Parabola seems to better represent the high flux points of *Fermi*. The following table summarizes the important values of both fits.

	Log Parabola	Smooth Broken Power Law
E_{peak} [GeV]	$(5.8951 \pm 2.5076) \times 10^1$	$(8.7723 \pm 10.1308) \times 10^1$
d.o.f	8	8
$\chi^2/d.o.f.$	7.869	8.304

In summary, the joint fit was easy to implement and therefore worked very successfully. The spectrum of PG1553+113 was shown to be in the range of IC scattering and π^0 decay. The use of several data sets from different instruments allows the generation of such models over a wide energy range. In future research, this will be a crucial element for further exploration of the production processes of γ -rays. In particular, the CTA can make an important contribution to this field with additional sensitivity in higher energy ranges. Another way to improve the model would be to consider data over a longer continuous time period. This could, for example, reduce errors like the one that occurred with the *Fermi* flux points.

List of Figures

1	The cosmic ray spectrum detectable on Earth	3
2	SED for the Leptonic and Hadronic Emission	6
3	Schematic illustration of a blazar with lepto-hadronic emission	8
4	All sky γ -ray map of <i>Fermi</i> -LAT for 60 months	9
5	EBL intensity and optical depth for different red shifts	11
6	<i>Fermi</i> Space Telescope in orbit of the earth	12
7	Schematic of the Fermi-LAT	13
8	Angle of the Cherenkov radiation	15
9	Cherenkov light initiated by a γ -ray	16
10	Counts maps of the ROI for 2019	25
11	$\sqrt{\text{TS}}$ and PS map of ROI for 2019	25
12	Average SED of PG1553+113 in 2019	26
13	Light curve of PG 1553+113 in 2019	28
14	Light curve of PG 1553+113 in 2019 with Bayesian Blocks.	29
15	Comparison of the SED estimated with FERMIPY and GAMMAPY	32
16	SED of PG1553+113 using H.E.S.S. data.	33
17	Combined illustration of the SEDs for the H.E.S.S. and <i>Fermi</i> data	34
18	Joint fit of a combined dataset using log parabola as spectral model	35
19	Joint fit of a combined dataset using smooth broken power law as spectral model	36
20	Configuration file for the FERMIPY analysis	45

List of Tables

1	Weekly binned light curve of PG1553+113 in 2019 using <i>Fermi</i> data	48
2	Light curve of PG1553+113 in 2019 with Bayesian Blocks	48
3	Flux Points of SED for 2019	49
4	Flux points of SED for period of H.E.S.S. observations estimated with FERMIPY	49
5	Flux points of SED for period of H.E.S.S. observations estimated with GAMMAPY	50
6	Flux points of SED using H.E.S.S. data	50

References

- Abdo, A. A. et al. (June 2010). “The Spectral Energy Distribution of Fermi Bright Blazars”. In: *Astrophysical Journal* 716.1, pp. 30–70. DOI: [10.1088/0004-637X/716/1/30](https://doi.org/10.1088/0004-637X/716/1/30). arXiv: [0912.2040 \[astro-ph.CO\]](https://arxiv.org/abs/0912.2040).
- Abdollahi, S. et al. (Mar. 2020). “Fermi Large Area Telescope Fourth Source Catalog”. In: *Astrophysical Journals* 247.1, 33, p. 33. DOI: [10.3847/1538-4365/ab6bcb](https://doi.org/10.3847/1538-4365/ab6bcb). arXiv: [1902.10045 \[astro-ph.HE\]](https://arxiv.org/abs/1902.10045).
- Abed, Yosef (2022). “Charakterisierung des Gammastrahlungs-Flares des Blazars PG 1553+113 im April 2019 mit H.E.S.S.” In.
- Abramowski, A. et al. (Mar. 2015). “The 2012 Flare of PG 1553+113 Seen with H.E.S.S. and Fermi-LAT”. In: *Astrophysical Journal* 802.1, 65, p. 65. DOI: [10.1088/0004-637X/802/1/65](https://doi.org/10.1088/0004-637X/802/1/65). arXiv: [1501.05087 \[astro-ph.HE\]](https://arxiv.org/abs/1501.05087).
- Ackermann, M. et al. (Mar. 2013). “Determination of the Point-spread Function for the Fermi Large Area Telescope from On-orbit Data and Limits on Pair Halos of Active Galactic Nuclei”. In: *Astrophysical Journal* 765.1, 54, p. 54. DOI: [10.1088/0004-637X/765/1/54](https://doi.org/10.1088/0004-637X/765/1/54). arXiv: [1309.5416 \[astro-ph.HE\]](https://arxiv.org/abs/1309.5416).
- Aharonian, F. et al. (Oct. 2004). “The Crab Nebula and Pulsar between 500 GeV and 80 TeV: Observations with the HEGRA Stereoscopic Air Cerenkov Telescopes”. In: *Astrophysical Journal* 614.2, pp. 897–913. DOI: [10.1086/423931](https://doi.org/10.1086/423931). arXiv: [astro-ph/0407118 \[astro-ph\]](https://arxiv.org/abs/astro-ph/0407118).
- Andrae, Rene, Tim Schulze-Hartung, and Peter Melchior (Dec. 2010). “Dos and don’ts of reduced chi-squared”. In: *arXiv e-prints*, arXiv:1012.3754, arXiv:1012.3754. DOI: [10.48550/arXiv.1012.3754](https://doi.org/10.48550/arXiv.1012.3754). arXiv: [1012.3754 \[astro-ph.IM\]](https://arxiv.org/abs/1012.3754).
- Atwood, W. B. et al. (June 2009). “The Large Area Telescope on the Fermi Gamma-Ray Space Telescope Mission”. In: *Astrophysical Journal* 697.2, pp. 1071–1102. DOI: [10.1088/0004-637X/697/2/1071](https://doi.org/10.1088/0004-637X/697/2/1071). arXiv: [0902.1089 \[astro-ph.IM\]](https://arxiv.org/abs/0902.1089).
- Becker, Julia K. (Mar. 2008). “High-energy neutrinos in the context of multimessenger astrophysics”. In: *Physics Reports* 458.4-5, pp. 173–246. DOI: [10.1016/j.physrep.2007.10.006](https://doi.org/10.1016/j.physrep.2007.10.006). arXiv: [0710.1557 \[astro-ph\]](https://arxiv.org/abs/0710.1557).
- Bruel, P. (Dec. 2021). “A new method to perform data-model comparison in Fermi-LAT analysis”. In: *Astronomy and Astrophysics* 656, A81, A81. DOI: [10.1051/0004-6361/202141553](https://doi.org/10.1051/0004-6361/202141553). arXiv: [2109.07443 \[astro-ph.HE\]](https://arxiv.org/abs/2109.07443).
- De Angelis, A. and M. Mallamaci (Aug. 2018). “Gamma-ray astrophysics”. In: *European Physical Journal Plus* 133.8, 324, p. 324. DOI: [10.1140/epjp/i2018-12181-0](https://doi.org/10.1140/epjp/i2018-12181-0). arXiv: [1805.05642 \[astro-ph.HE\]](https://arxiv.org/abs/1805.05642).

- de Naurois, Mathieu and H. E. S. S. Collaboration (Apr. 2019). “H.E.S.S. detects high VHE gamma-ray flux in PG 1553+113”. In: *The Astronomer’s Telegram* 12641, p. 1.
- Degrange, Bernard and Gérard Fontaine (Aug. 2015). “Introduction to high-energy gamma-ray astronomy”. In: *Comptes Rendus Physique* 16.6-7, pp. 587–599. DOI: [10.1016/j.crhy.2015.07.003](https://doi.org/10.1016/j.crhy.2015.07.003). arXiv: [1604.05488](https://arxiv.org/abs/1604.05488) [astro-ph.HE].
- Deil, C. et al. (July 2017). “Gammapy - A prototype for the CTA science tools”. In: *35th International Cosmic Ray Conference (ICRC2017)*. Vol. 301. International Cosmic Ray Conference, 766, p. 766. DOI: [10.22323/1.301.0766](https://doi.org/10.22323/1.301.0766). arXiv: [1709.01751](https://arxiv.org/abs/1709.01751) [astro-ph.IM].
- Dominguez, A. et al. (Feb. 2011). “Extragalactic background light inferred from AEGIS galaxy-SED-type fractions”. In: *Monthly Notices of the Royal Astronomical Society* 410.4, pp. 2556–2578. DOI: [10.1111/j.1365-2966.2010.17631.x](https://doi.org/10.1111/j.1365-2966.2010.17631.x). arXiv: [1007.1459](https://arxiv.org/abs/1007.1459) [astro-ph.CO].
- Dorigo Jones, J. et al. (Jan. 2022). “Improving blazar redshift constraints with the edge of the Ly α forest: 1ES 1553+113 and implications for observations of the WHIM”. In: *Monthly Notices of the Royal Astronomical Society* 509.3, pp. 4330–4343. DOI: [10.1093/mnras/stab3331](https://doi.org/10.1093/mnras/stab3331). arXiv: [2111.06927](https://arxiv.org/abs/2111.06927) [astro-ph.GA].
- Dwek, Eli and Frank Krennrich (Mar. 2013). “The extragalactic background light and the gamma-ray opacity of the universe”. In: *Astroparticle Physics* 43, pp. 112–133. DOI: [10.1016/j.astropartphys.2012.09.003](https://doi.org/10.1016/j.astropartphys.2012.09.003). arXiv: [1209.4661](https://arxiv.org/abs/1209.4661) [astro-ph.CO].
- Evoli, Carmelo (Dec. 2020). *The Cosmic-Ray Energy Spectrum*. DOI: [10.5281/zenodo.4396125](https://doi.org/10.5281/zenodo.4396125). URL: <https://doi.org/10.5281/zenodo.4396125>.
- Fermi-LAT Collaboration et al. (Nov. 2018). “A gamma-ray determination of the Universe’s star formation history”. In: *Science* 362.6418, pp. 1031–1034. DOI: [10.1126/science.aat8123](https://doi.org/10.1126/science.aat8123). arXiv: [1812.01031](https://arxiv.org/abs/1812.01031) [astro-ph.HE].
- Funk, Stefan (Oct. 2015). “Ground- and Space-Based Gamma-Ray Astronomy”. In: *Annual Review of Nuclear and Particle Science* 65, pp. 245–277. DOI: [10.1146/annurev-nucl-102014-022036](https://doi.org/10.1146/annurev-nucl-102014-022036). arXiv: [1508.05190](https://arxiv.org/abs/1508.05190) [astro-ph.HE].
- Goddard Space Flight Center (Feb. 2013). *Observatories Across the Electromagnetic Spectrum*. URL: https://imagine.gsfc.nasa.gov/science/toolbox/emspectrum_observatories1.html. (accessed: 10.04.2023).
- Green, R. F., M. Schmidt, and J. Liebert (June 1986). “The Palomar-Green Catalog of Ultraviolet-Excess Stellar Objects”. In: *Astrophysical Journals* 61, p. 305. DOI: [10.1086/191115](https://doi.org/10.1086/191115).

- H.E.S.S. Collaboration (Oct. 2016). *PKS 2155-304 - a Beethoven among blazars*. Last accessed 10 April 2023. URL: <https://www.mpi-hd.mpg.de/hfm/HESS/pages/home/som/2016/10/#Ref3>.
- (2021). *High Energy Stereoscopic System*. Last accessed 22 February 2023. URL: <https://www.mpi-hd.mpg.de/HESS/pages/about/>.
- Hewitt, A. and G. Burbidge (Jan. 1987). “A New Optical Catalog of Quasi-stellar Objects”. In: *Astrophysical Journals* 63, p. 1. DOI: [10.1086/191163](https://doi.org/10.1086/191163).
- Hinton, J. A. and W. Hofmann (Sept. 2009). “Teraelectronvolt Astronomy”. In: 47.1. Provided by the SAO/NASA Astrophysics Data System, pp. 523–565. DOI: [10.1146/annurev-astro-082708-101816](https://doi.org/10.1146/annurev-astro-082708-101816). eprint: [1006.5210](https://ui.adsabs.harvard.edu/abs/2009ARA&A..47..523H). URL: <https://ui.adsabs.harvard.edu/abs/2009ARA&A..47..523H>.
- Jelley, J. V. (July 1955). “SPECIAL ARTICLE: Cerenkov radiation and its applications”. In: *British journal of Applied Physics* 6.7, pp. 227–232. DOI: [10.1088/0508-3443/6/7/301](https://doi.org/10.1088/0508-3443/6/7/301).
- Joshi, M., A. P. Marscher, and M. Böttcher (Apr. 2014). “Seed Photon Fields of Blazars in the Internal Shock Scenario”. In: *Astrophysical Journal* 785.2, 132, p. 132. DOI: [10.1088/0004-637X/785/2/132](https://doi.org/10.1088/0004-637X/785/2/132). arXiv: [1403.1354](https://arxiv.org/abs/1403.1354) [astro-ph.HE].
- Lipari, Paolo (Feb. 2021). “The origin of the power-law form of the extragalactic gamma-ray flux”. In: *Astroparticle Physics* 125, 102507, p. 102507. DOI: [10.1016/j.astropartphys.2020.102507](https://doi.org/10.1016/j.astropartphys.2020.102507). arXiv: [2001.00982](https://arxiv.org/abs/2001.00982) [astro-ph.HE].
- Matthews, James H., Anthony R. Bell, and Katherine M. Blundell (Sept. 2020). “Particle acceleration in astrophysical jets”. In: *New Astronomy Review* 89, 101543, p. 101543. DOI: [10.1016/j.newar.2020.101543](https://doi.org/10.1016/j.newar.2020.101543). arXiv: [2003.06587](https://arxiv.org/abs/2003.06587) [astro-ph.HE].
- NASA (Nov. 2022). *Fermitools: Cicerone*. URL: <https://fermi.gsfc.nasa.gov/ssc/data/analysis/documentation/Cicerone/>. (accessed: 17.03.2023).
- Romero, Gustavo E. et al. (2018). “Relativistic Jets in Active Galactic Nuclei and Microquasars”. In: *Jets and Winds in Pulsar Wind Nebulae*. Ed. by Andrei Bykov et al. Vol. 62, pp. 5–61. DOI: [10.1007/978-94-024-1292-5_2](https://doi.org/10.1007/978-94-024-1292-5_2).
- Scargle, Jeffrey D. (Sept. 1998). “Studies in Astronomical Time Series Analysis. V. Bayesian Blocks, a New Method to Analyze Structure in Photon Counting Data”. In: *Astrophysical Journal* 504.1, pp. 405–418. DOI: [10.1086/306064](https://doi.org/10.1086/306064). arXiv: [astro-ph/9711233](https://arxiv.org/abs/astro-ph/9711233) [astro-ph].
- Scargle, Jeffrey D. et al. (Feb. 2013). “Studies in Astronomical Time Series Analysis. VI. Bayesian Block Representations”. In: *Astrophysical Journal* 764.2, 167, p. 167. DOI: [10.1088/0004-637X/764/2/167](https://doi.org/10.1088/0004-637X/764/2/167). arXiv: [1207.5578](https://arxiv.org/abs/1207.5578) [astro-ph.IM].

- Schmidt, M. R. (1963). “3C 273 : A Star-Like Object with Large Red-Shift”. In: *Nature* 197, pp. 1040–1040.
- Soheila, Abdollahi et al. (Jan. 2023). “The Fermi-LAT Light Curve Repository”. In: *arXiv e-prints*, arXiv:2301.01607, arXiv:2301.01607. DOI: [10.48550/arXiv.2301.01607](https://doi.org/10.48550/arXiv.2301.01607), arXiv: [2301.01607](https://arxiv.org/abs/2301.01607) [astro-ph.HE].
- Stern, David P (Nov. 2003). *The Exploration of the Earth’s Magnetosphere*. URL: <https://pwg.gsfc.nasa.gov/Education/Intro.html>. (accessed: 07.04.2023).
- The Open University (Sept. 2019). *Introduction to active galaxies*. URL: <https://www.open.edu/openlearn/science-maths-technology/introduction-active-galaxies>. (accessed: 07.03.2023).
- Thompson, A. Richard, James M. Moran, and Jr. Swenson George W. (2017). “Interferometry and Synthesis in Radio Astronomy, 3rd Edition”. In: chap. 5.3. DOI: [10.1007/978-3-319-44431-4](https://doi.org/10.1007/978-3-319-44431-4).
- Unbehaun, Tim (2020). “Joint-instrument analyses with Gammapy”. In.
- Wilks, S. S. (1938). “The Large-Sample Distribution of the Likelihood Ratio for Testing Composite Hypotheses”. In: *The Annals of Mathematical Statistics* 9.1, pp. 60–62. ISSN: 00034851. URL: <http://www.jstor.org/stable/2957648> (visited on 03/15/2023).
- Wood, M. et al. (July 2017). “Fermipy: An open-source Python package for analysis of Fermi-LAT Data”. In: *35th International Cosmic Ray Conference (ICRC2017)*. Vol. 301. International Cosmic Ray Conference, 824, p. 824. DOI: [10.22323/1.301.0824](https://doi.org/10.22323/1.301.0824), arXiv: [1707.09551](https://arxiv.org/abs/1707.09551) [astro-ph.IM].

Appendix

```

1 data:
2   evfile : evfile.txt
3   scfile : scfile.fits
4   ltcube: null
5 binning:
6   roiwidth  : 10.0
7   binsz     : 0.1
8   binsperdec : 8
9 selection :
10  emin : 100 #MeV
11  emax : 316227.76 #MeV
12  zmax  : 90 #deg
13  evclass : 128
14  evtype  : 3
15  tmin   : 567993605 # 2019-01-01 00:00:00
16  tmax   : 599443204 # 2019-12-30 23:59:59
17  filter : 'DATA_QUAL>0 && LAT_CONFIG==1'
18  target : 'pg1553+113'
19 gtlike:
20  edisp : True
21  irfs  : 'P8R3_SOURCE_V3'
22  edisp_disable : ['isodiff','galdiff']
23 model:
24  src_roiwidth : 15.0
25  galdiff      : 'gll_iem_v07.fits'
26  isodiff     : 'iso_P8R3_SOURCE_V3_v1.txt'
27  catalogs    : ['gll_psc_v30.fit']

```

Figure 20: Configuration file for the FERMIPY analysis. The file includes all settings made for the analysis. The period of time was changed for the combined fit to the period of H.E.S.S. observations

The following steps show the calculation of the energy peak of the SED assuming a Log Parabola as spectral model:

$$\frac{dS(E)}{dE} = \frac{d}{dE} \left[N_0 E^2 \cdot \left(\frac{E}{E_0} \right)^{-\alpha - \beta \ln \left(\frac{E}{E_0} \right)} \right] \quad (32)$$

$$\begin{aligned} &= 2N_0 E \cdot \left(\frac{E}{E_0} \right)^{-\alpha - \beta \ln \left(\frac{E}{E_0} \right)} \\ &\quad - N_0 E^2 \cdot \left(\frac{E}{E_0} \right)^{-\alpha - \beta \ln \left(\frac{E}{E_0} \right)} \left(\frac{\alpha + \beta \ln \left(\frac{E}{E_0} \right)}{E} + \frac{\beta \ln \left(\frac{E}{E_0} \right)}{E} \right) \\ &= N_0 E \cdot \left(\frac{E}{E_0} \right)^{-\alpha - \beta \ln \left(\frac{E}{E_0} \right)} \left(2 - \alpha - 2\beta \ln \left(\frac{E}{E_0} \right) \right) \end{aligned}$$

$$\begin{aligned} \frac{dS(E)}{dE} \stackrel{!}{=} 0 &\Leftrightarrow 0 = 2 - \alpha - 2\beta \ln \left(\frac{E}{E_0} \right) \quad (33) \\ &\Leftrightarrow E_{\text{peak,LP}} = E_0 e^{\frac{2-\alpha}{2\beta}} \end{aligned}$$

It follows the calculation of the energy peak of the SED assuming a Smooth Broken Power Law as spectral model:

$$\begin{aligned} \frac{dS(E)}{dE} &= \frac{d}{dE} \left[N_0 E^2 \left(\frac{E}{E_0} \right)^{-\gamma_1} \left(\left(\frac{E}{E_b} \right)^{\frac{\gamma_2 - \gamma_1}{\beta}} + 1 \right)^{-\beta} \right] \quad (34) \\ &= - \frac{N_0 \gamma_1 E}{\left(\frac{E}{E_0} \right)^{\gamma_1} \left(\left(\frac{E}{E_b} \right)^{\frac{\gamma_2 - \gamma_1}{\beta}} + 1 \right)^\beta} + \frac{2N_0 E}{\left(\frac{E}{E_0} \right)^{\gamma_1} \left(\left(\frac{E}{E_b} \right)^{\frac{\gamma_2 - \gamma_1}{\beta}} + 1 \right)^\beta} \\ &\quad - \frac{N_0 \cdot (\gamma_2 - \gamma_1) E \cdot \left(\frac{E}{E_b} \right)^{\frac{\gamma_2 - \gamma_1}{\beta}}}{\left(\frac{E}{E_0} \right)^{\gamma_1} \left(\left(\frac{E}{E_b} \right)^{\frac{\gamma_2 - \gamma_1}{\beta}} + 1 \right)^{\beta+1}} \\ &= - \frac{N_0 E \left((\gamma_2 - 2) \cdot \left(\frac{E}{E_b} \right)^{\frac{\gamma_2 - \gamma_1}{\beta}} + \gamma_1 - 2 \right)}{\left(\frac{E}{E_0} \right)^{\gamma_1} \left(\left(\frac{E}{E_b} \right)^{\frac{\gamma_2 - \gamma_1}{\beta}} + 1 \right)^{\beta+1}} \end{aligned}$$

$$\begin{aligned}
\frac{dS(E)}{dE} \stackrel{!}{=} 0 &\Leftrightarrow 0 = (\gamma_2 - 2) \cdot \left(\frac{E}{E_b}\right)^{\frac{\gamma_2 - \gamma_1}{\beta}} + \gamma_1 - 2 & (35) \\
&\Leftrightarrow \left(\frac{E}{E_b}\right)^{\frac{\gamma_2 - \gamma_1}{\beta}} = \frac{2 - \gamma_1}{\gamma_2 - 2} \\
&\Leftrightarrow E_{\text{peak,SBPL}} = E_b \cdot \left(\frac{2 - \gamma_1}{\gamma_2 - 2}\right)^{\frac{\beta}{\gamma_2 - \gamma_1}}
\end{aligned}$$

Week	t_{\min} [date]	t_{\max} [date]	dN/dE [$10^{-8} \text{ s}^{-1} \text{ cm}^{-2}$]	σ [$10^{-8} \text{ s}^{-1} \text{ cm}^{-2}$]
1	2019-01-01	2019-01-08	11.940	2.665
2	2019-01-08	2019-01-15	9.323	1.979
3	2019-01-15	2019-01-22	13.910	2.452
4	2019-01-22	2019-01-29	14.495	2.656
5	2019-01-29	2019-02-05	10.618	1.841
6	2019-02-05	2019-02-12	8.546	1.660
7	2019-02-12	2019-02-19	6.034	1.482
8	2019-02-19	2019-02-26	8.335	2.015
9	2019-02-26	2019-03-05	15.509	2.905
10	2019-03-05	2019-03-12	8.004	2.707
11	2019-03-12	2019-03-19	10.671	2.251
12	2019-03-19	2019-03-26	13.831	2.903
13	2019-03-26	2019-04-02	10.864	2.674
14	2019-04-02	2019-04-09	15.571	2.383
15	2019-04-09	2019-04-16	11.590	3.148
16	2019-04-16	2019-04-23	14.111	3.563
17	2019-04-23	2019-04-30	10.574	2.335
18	2019-04-30	2019-05-07	8.601	2.477
19	2019-05-07	2019-05-14	9.681	2.242
20	2019-05-14	2019-05-21	5.300	2.659
21	2019-05-21	2019-05-28	6.408	2.458
22	2019-05-28	2019-06-04	7.606	3.579
23	2019-06-04	2019-06-11	7.058	2.710
24	2019-06-11	2019-06-18	5.017	2.596
25	2019-06-18	2019-06-25	6.967	2.067
26	2019-06-25	2019-07-02	7.487	2.076
27	2019-07-02	2019-07-09	5.741	2.283
28	2019-07-09	2019-07-16	6.935	1.827

Week	t_{\min} [date]	t_{\max} [date]	dN/dE [$10^{-8} \text{ s}^{-1} \text{ cm}^{-2}$]	σ [$10^{-8} \text{ s}^{-1} \text{ cm}^{-2}$]
29	2019-07-16	2019-07-23	8.437	2.194
30	2019-07-23	2019-07-30	8.323	1.804
31	2019-07-30	2019-08-06	8.564	2.977
32	2019-08-06	2019-08-13	9.451	2.137
33	2019-08-13	2019-08-20	5.339	1.827
34	2019-08-20	2019-08-27	10.128	2.144
35	2019-08-27	2019-09-03	6.985	2.193
36	2019-09-03	2019-09-10	8.537	2.233
37	2019-09-10	2019-09-17	6.835	2.202
38	2019-09-17	2019-09-24	6.841	2.007
39	2019-09-24	2019-10-01	4.690	1.371
40	2019-10-01	2019-10-08	1.694	2.551
41	2019-10-08	2019-10-15	3.963	1.523
42	2019-10-15	2019-10-22	5.631	1.675
43	2019-10-22	2019-10-29	4.206	1.573
44	2019-10-29	2019-11-05	5.555	1.834
45	2019-11-05	2019-11-12	7.135	1.885
46	2019-11-12	2019-11-19	7.820	2.169
47	2019-11-19	2019-11-26	9.816	2.639
48	2019-11-26	2019-12-03	1.923	2.244
49	2019-12-03	2019-12-10	6.738	2.918
50	2019-12-10	2019-12-17	5.458	2.759
51	2019-12-17	2019-12-24	8.424	2.128
52	2019-12-24	2019-12-31	4.520	1.735

Table 1: Weekly binned light curve of PG1553+113 in 2019 using *Fermi* data. The flux dN/dE is shown for each week.

Bin	t_{\min} [date]	t_{\max} [date]	dN/dE [$10^{-8} \text{ s}^{-1} \text{ cm}^{-2}$]	σ [$10^{-8} \text{ s}^{-1} \text{ cm}^{-2}$]
1	2019-01-04	2019-03-12	10.816	0.741
2	2019-03-12	2019-04-23	12.625	1.194
3	2019-04-23	2019-07-09	7.381	0.793
4	2019-07-09	2019-07-23	7.869	1.445
5	2019-07-23	2019-12-27	7.184	0.467

Table 2: Light curve of PG1553+113 in 2019 with Bayesian Blocks using *Fermi* data. The bins were estimated by performing the Bayesian Block algorithm.

E_{\min} [MeV]	E_{\max} [MeV]	$S(E)$ [10^{-5} MeV s $^{-1}$ cm $^{-2}$]	σ_S [10^{-5} MeV s $^{-1}$ cm $^{-2}$]
100	177.828	0.799	0.127
177.828	316.228	0.626	0.098
316.228	562.341	0.615	0.085
562.341	1000	1.012	0.094
1000	1778.279	1.394	0.113
1778.279	3162.278	1.824	0.153
3162.278	5623.413	2.768	0.238
5623.413	10000	2.720	0.307
10000	17782.794	3.269	0.444
17782.794	31622.777	3.852	0.633
31622.777	56234.133	5.140	0.955
56234.133	100000	5.725	1.353
100000	177827.941	3.919	1.507
177827.941	316227.766	1.037	1.043

Table 3: Flux points of the SED of PG1553+113 for 2019 using *Fermi* data. Analysis performed with FERMIPY.

E_{\min} [MeV]	E_{\max} [MeV]	$S(E)$ [10^{-5} MeV s $^{-1}$ cm $^{-2}$]	σ_S [10^{-5} MeV s $^{-1}$ cm $^{-2}$]
1	1.778	2.489	0.525
1.778	3.162	1.921	0.581
3.162	5.623	4.75	1.084
5.623	10	3.671	1.253
10	17.782	5.527	2.108
17.782	31.622	4.943	2.583
31.622	56.234	4.367	3.116
56.234	100	14.200 (upper limit)	4.868
100	177.827	20.979	12.194
177.827	316.227	17.327 (upper limit)	6.404

Table 4: Flux points of the SED of PG1553+113 for the period of the H.E.S.S. observations using *Fermi* data. Analysis performed with FERMIPY.

E_{\min} [MeV]	E_{\max} [MeV]	$S(E)$ [10^{-5} MeV s $^{-1}$ cm $^{-2}$]	σ_S [10^{-5} MeV s $^{-1}$ cm $^{-2}$]
1	1.778	2.304	0.519
1.778	3.162	1.819	0.580
3.162	5.623	4.601	1.105
5.623	10	3.623	1.264
10	17.782	5.425	2.109
17.782	31.622	4.588	2.583
31.622	56.234	4.112	3.129
56.234	100	14.107(upper limit)	5.353
100	177.827	20.986	12.276
177.827	316.227	25.551(upper limit)	6.388

Table 5: Flux points of the SED of PG1553+113 for the period of the H.E.S.S. observations using *Fermi* data. Analysis performed with GAMMAPY.


E_{\min} [TeV]	E_{\max} [TeV]	$S(E)$ [MeV s $^{-1}$ cm $^{-2}$]	σ_S [MeV s $^{-1}$ cm $^{-2}$]
0.251	0.316	1.250×10^{-5}	4.066×10^{-6}
0.316	0.398	4.650×10^{-6}	3.730×10^{-7}
0.398	0.501	2.209×10^{-6}	2.509×10^{-7}
0.501	0.631	1.093×10^{-6}	1.633×10^{-7}
0.631	0.794	2.290×10^{-7}	9.325×10^{-8}
0.794	1.584	6.555×10^{-8}	3.056×10^{-8}

Table 6: Flux points of the SED of PG1553+113 for the period of the H.E.S.S. observations using H.E.S.S. data. Analysis performed with GAMMAPY.

Eidesstattliche Erklärung

Ich versichere an Eides statt, dass ich die vorstehende Arbeit selbständig und ohne fremde Hilfe angefertigt und mich anderer als der im beigefügten Verzeichnis angegebenen Hilfsmittel nicht bedient habe. Alle Stellen, die wörtlich oder sinngemäß aus Veröffentlichungen übernommen wurden, sind als solche kenntlich gemacht. Alle Internetquellen sind der Arbeit beigefügt. Des Weiteren versichere ich, dass ich die Arbeit vorher nicht in einem anderen Prüfungsverfahren eingereicht habe und dass die eingereichte schriftliche Fassung der elektronischen Fassung entspricht.

Hamburg, 18.04.2023

A handwritten signature in black ink, consisting of a large, stylized initial 'J' followed by a cursive name.

Unterschrift